

# 1 **Allosteric activation or inhibition of PI3K $\gamma$ mediated through** 2 **conformational changes in the p110 $\gamma$ helical domain**

3  
4 Noah J Harris<sup>1\*</sup>, Meredith L Jenkins<sup>1\*</sup>, Sung-Eun Nam<sup>2</sup> Manoj K Rathinaswamy<sup>1</sup>,  
5 Matthew AH Parson<sup>1</sup>, Harish Ranga-Prasad<sup>1</sup>, Udit Dalwadi<sup>2</sup>, Brandon E Moeller<sup>1</sup>,  
6 Eleanor Sheekey<sup>1</sup>, Scott D Hansen<sup>3</sup>, Calvin K Yip<sup>2%</sup>, and John E Burke<sup>1,2%</sup>

7  
8  
9 <sup>1</sup>Department of Biochemistry and Microbiology, University of Victoria, Victoria, British  
10 Columbia, V8W 2Y2, Canada

11 <sup>2</sup>Department of Biochemistry and Molecular Biology, The University of British Columbia,  
12 Vancouver, British Columbia V6T 1Z3, Canada

13 <sup>3</sup>Department of Chemistry and Biochemistry, Institute of Molecular Biology, University of  
14 Oregon, Eugene, OR 97403

15  
16 \*These authors contributed equally

17 <sup>%</sup>To whom correspondence should be addressed: John E. Burke

18 Tel: 1-250-721-8732, email: jeburke@uvic.ca

19 Calvin K. Yip

20 Tel: 1-604-827-3976, email: calvin.yip@ubc.ca

21  
22  
23 **Keywords:** PI3K, PIK3CG, PI3K $\gamma$ , p110 $\gamma$ , p101, p84, PIK3R5, PIK3R6, phosphoinositide  
24 3-kinase, hydrogen exchange, protein kinase C, PKC, nanobodies.

25  
26  
27  
28  
29  
30 **Abstract**

31 PI3K $\gamma$  is a critical immune signaling enzyme activated downstream of diverse cell  
32 surface molecules, including Ras, PKC $\beta$  activated by the IgE receptor, and G $\beta\gamma$   
33 subunits released from activated GPCRs. PI3K $\gamma$  can form two distinct complexes, with  
34 the p110 $\gamma$  catalytic subunit binding to either a p101 or p84 regulatory subunit, with these  
35 complexes being differentially activated by upstream stimuli. Here using a combination  
36 of cryo electron microscopy, HDX-MS, and biochemical assays we have identified novel  
37 roles of the helical domain of p110 $\gamma$  in regulating lipid kinase activity of distinct PI3K $\gamma$   
38 complexes. We defined the molecular basis for how an allosteric inhibitory nanobody  
39 potently inhibits kinase activity through rigidifying the helical domain and regulatory  
40 motif of the kinase domain. The nanobody did not block either p110 $\gamma$  membrane  
41 recruitment or Ras/G $\beta\gamma$  binding, but instead decreased ATP turnover. We also identified  
42 that p110 $\gamma$  can be activated by dual PKC $\beta$  helical domain phosphorylation leading to  
43 partial unfolding of an N-terminal region of the helical domain. PKC $\beta$  phosphorylation is  
44 selective for p110 $\gamma$ -p84 compared to p110 $\gamma$ -p101, driven by differential dynamics of the  
45 helical domain of these different complexes. Nanobody binding prevented PKC $\beta$   
46 mediated phosphorylation. Overall, this work shows an unexpected allosteric  
47 regulatory role of the helical domain of p110 $\gamma$  that is distinct between p110 $\gamma$ -p84 and  
48 p110 $\gamma$ -p101 and reveals how this can be modulated by either phosphorylation or  
49 allosteric inhibitory binding partners. This opens possibilities of future allosteric inhibitor  
50 development for therapeutic intervention.

51

52

## 53 Introduction

54 The class I phosphoinositide 3 kinases (PI3Ks) are master regulators of myriad  
55 functions through their generation of the lipid signalling molecule phosphatidylinositol  
56 3,4,5-trisphosphate (PIP<sub>3</sub>) downstream of cell surface receptors (Burke and Williams,  
57 2015; Rathinaswamy and Burke, 2019; Vanhaesebroeck et al., 2021; Vasan and  
58 Cantley, 2022). The class I PI3Ks can be further subdivided into the class IA and class  
59 IB subfamilies, with class IB PI3Ks being critical in immune signalling, and are  
60 composed of a single p110 $\gamma$  catalytic subunit that can bind to either a p101 or p84  
61 regulatory subunit (Hawkins and Stephens, 2015; Lanahan et al., 2022; Okkenhaug,  
62 2013). The two PI3K $\gamma$  complexes (either p110 $\gamma$ -p84 or p110 $\gamma$ -p101) play essential and  
63 independent roles in both the adaptative and innate immune systems. PI3K $\gamma$  has shown  
64 promise as a therapeutic target, primarily as an immunomodulator of the tumor  
65 microenvironment leading to enhanced anti-tumor immune responses (De Henau et al.,  
66 2016; Kaneda et al., 2016b). Multiple isoform selective small molecule ATP competitive  
67 inhibitors of p110 $\gamma$  are in clinical trials for multiple forms of human cancers (Li et al.,  
68 2021). However, all inhibitors currently developed towards p110 $\gamma$  act as ATP  
69 competitive inhibitors, showing equal potency against both p110 $\gamma$ -p84 or p110 $\gamma$ -p101  
70 complexes.

71 Detailed experiments on the role of p110 $\gamma$  in mice show that knockout of both  
72 p101 and p84 leads to PIP<sub>3</sub> levels that are equivalent to knockout of p110 $\gamma$ , showing  
73 that all cellular PI3K $\gamma$  activity requires the presence of either a p84 or p101 regulatory  
74 subunit (Rynkiewicz et al., 2020). The two complexes are differentially activated by  
75 membrane localised receptors, including G-protein coupled receptors (Li et al., 2000;  
76 Stephens et al., 1997), Ras (Jin et al., 2020; Kurig et al., 2009), toll like receptors  
77 (TLRs) (Luo et al., 2018), and the IgE antigen receptor (Laffargue et al., 2002; Walser et  
78 al., 2013). This leads to the different complexes driving unique immune responses, with  
79 p110 $\gamma$ -p101 involved in chemotaxis in neutrophils (Bohnacker et al., 2009; Deladeriere et  
80 al., 2015), and p110 $\gamma$ -p84 involved in reactive oxide production. Differential activation of  
81 unique PI3K $\gamma$  complexes downstream of GPCRs and Ras is caused by the ability of  
82 p101 to directly bind to G $\beta\gamma$  subunits downstream of activated GPCRs, with this being

83 lost in p84, making p110 $\gamma$ -p84 activation by G $\beta\gamma$  dependent on Ras mediated  
84 membrane recruitment (Rathinaswamy et al., 2023; Kurig et al., 2009; Rynkiewicz et al.,  
85 2020). Activation of PI3K $\gamma$  downstream of the IgE antigen receptor is driven by calcium  
86 mediated activation of protein kinase C $\beta$ , leading to the selective phosphorylation and  
87 activation of p110 $\gamma$  at S582 (Walser et al., 2013), with this putatively only occurring in  
88 p110 $\gamma$ -p84 and not p110 $\gamma$ -p101. The full molecular mechanisms underlying how  
89 phosphorylation of p110 $\gamma$  is selective for different p84 or p101 complexes, and how it  
90 activates lipid kinase activity are poorly understood.

91         Extensive biophysical approaches including cryo electron microscopy (cryo-EM),  
92 X-ray crystallography, and hydrogen deuterium exchange mass spectrometry (HDX-  
93 MS) have provided extensive insight into the molecular underpinnings of how p110 $\gamma$   
94 associates with both p101 and p84, how they are differentially activated by Ras and  
95 GPCR signals, and how they can be activated on lipid membranes (Pacold et al., 2000;  
96 Walker et al., 1999; Rathinaswamy et al., 2021c, 2021a; Gangadhara et al., 2019;  
97 Vadas et al., 2013; Rathinaswamy et al., 2023). The p110 $\gamma$  catalytic subunit is  
98 composed of an adaptor binding domain (ABD), a Ras binding domain (RBD), a C2  
99 domain, a helical domain, and a bi-lobal kinase domain (Rathinaswamy et al., 2021a;  
100 Walker et al., 1999). A set of helices positioned C-terminal to the activation loop in the  
101 kinase domain play a critical role in regulating activity, with this region referred to as the  
102 regulatory motif (Rathinaswamy et al., 2021c). The p110 $\gamma$  isoform is unique in that it is  
103 inhibited in the absence of a regulatory subunit, with this driven by an autoinhibitory  
104 conformation of the regulatory motif, that is proposed to require membrane association  
105 to disrupt (Gangadhara et al., 2019). The regulatory motif is a common site of activating  
106 mutations in the other class I PI3K isoforms (Jenkins et al., 2023), with p110 $\gamma$  having  
107 rare activating oncogenic mutants in this region (Rathinaswamy et al., 2021c). The  
108 p110 $\gamma$  subunit interacts with both p84 and p101 at an interface composed of the C2  
109 domain, and the linkers between the RBD-C2 and C2-helical domains (Rathinaswamy  
110 et al., 2023, 2021a). The p110 $\gamma$ -p84 complex forms a more dynamic complex compared  
111 to p110 $\gamma$ -p101 (Rathinaswamy et al., 2023; Shymanets et al., 2013), however, no clear  
112 unique regulatory role of this difference in dynamics has been identified.



113 The fundamental roles of p110 $\gamma$  in inflammatory processes has made it a  
114 therapeutic target in many pathological conditions, including asthma (Campa et al.,  
115 2018), arthritis (Camps et al., 2005), obesity (Becattini et al., 2011; Breasson et al.,  
116 2017), and cancer (De Henau et al., 2016; Kaneda et al., 2016a, 2016b). There are  
117 significant side effects from non-isoform selective PI3K inhibitors (Bohnacker et al.,  
118 2017; Vanhaesebroeck et al., 2021), which has driven the development of highly p110 $\gamma$   
119 selective small molecule inhibitors (Bell et al., 2012; Evans et al., 2016; Gangadhara et  
120 al., 2019). However, all p110 $\gamma$  inhibitors will target both p110 $\gamma$ -p101 and p110 $\gamma$ -p84, so  
121 there is a potential for the development of allosteric inhibitors outside of the ATP binding  
122 site. Initial promise has been reported for the development of class IA p110 $\alpha$  oncogene  
123 specific allosteric inhibitors. However, further investigation of the molecular mechanisms  
124 underlying p110 $\gamma$  regulation will be required for the discovery of regions that can be  
125 targeted for allosteric inhibitor development.

126 Here we report critical roles of the helical domain of p110 $\gamma$  in both activation and  
127 inhibition of lipid kinase activity. We characterised an allosteric inhibitory nanobody  
128 (NB7) that potently inhibits p110 $\gamma$  activity. Cryo-EM was used to define the inhibitory  
129 interface, which is composed of the helical domain, the ABD-RBD linker, and the  
130 regulatory motif of the kinase domain of p110 $\gamma$ . The region that the nanobody binds to is  
131 in close spatial proximity to a previously identified PKC $\beta$  phosphorylation site (S582) in  
132 the helical domain, and oncogenic activating mutants in the regulatory motif. We fully  
133 characterised the activity and dynamics of stoichiometrically PKC $\beta$  phosphorylated  
134 p110 $\gamma$ , leading to the discovery of a novel additional phosphorylation site (either S594 or  
135 S595). PKC $\beta$  phosphorylation was highly selective for p110 $\gamma$  and p110 $\gamma$ -p84, with  
136 limited phosphorylation of p110 $\gamma$ -p101. Hydrogen deuterium exchange mass  
137 spectrometry (HDX-MS) analysis showed that phosphorylation of p110 $\gamma$  leads to  
138 unfolding of the N-terminal region of the helical domain, and increased kinase activity.  
139 The presence of the inhibitory nanobody significantly blocks PKC $\beta$  phosphorylation,  
140 while phosphorylation of p110 $\gamma$  prevented binding to NB7. Overall, this work provides  
141 unique insight into the critical role of the helical domain in controlling p110 $\gamma$  activity, and  
142 how phosphorylation and binding partners can modify this regulation. It also reveals a

143 unique binding site located at the interface of the helical and kinase domain that can be  
144 targeted for future allosteric inhibitor design.

145

## 146 **Results**

### 147 *Molecular mechanism of nanobody inhibition of p110 $\gamma$*

148 We previously identified multiple nanobodies that inhibited the activity of p110 $\gamma$ .  
149 One from this group (denoted NB7 throughout the manuscript) potently inhibited the  
150 membrane mediated activation of p110 $\gamma$ -p84 by both Ras and G $\beta\gamma$ , with HDX-MS  
151 experiments mapping the NB7 binding interface to the RBD, helical and kinase domains  
152 (Rathinaswamy et al., 2021b). We originally hypothesized that NB7 worked by sterically  
153 inhibiting Ras binding to the RBD domain of p110 $\gamma$ . To further explore the molecular  
154 mechanism of inhibition we purified all complexes of p110 $\gamma$  (p110 $\gamma$  apo, p110 $\gamma$ -p84,  
155 p110 $\gamma$ -p101) along with the NB7 nanobody. The SDS-PAGE of all proteins utilised in  
156 this study are shown in the source data file included in the supplemental information.

157 To define the mechanism concerning how NB7 inhibits PI3K activity we analyzed  
158 how this nanobody inhibited all class IB PI3K complexes (p110 $\gamma$ , p110 $\gamma$ -p84, p110 $\gamma$ -  
159 p101) upon activation by lipidated G $\beta\gamma$  subunits. Intriguingly, we found that all three  
160 forms of p110 $\gamma$  were potently inhibited by NB7 (Fig. 1A). While the IC<sub>50</sub> measured for  
161 the three complexes was different, this is likely mainly due to the dramatic difference in  
162 protein required to measure lipid kinase activity *in vitro* (~300 nM for p110 $\gamma$  apo/p110 $\gamma$ -  
163 p84, and ~10 nM for p110 $\gamma$ -p101, respectively). This suggested that the mechanism of  
164 inhibition was not driven by a steric block of Ras association through the RBD, as  
165 previously proposed (Rathinaswamy et al., 2021b). We examined the binding of this  
166 nanobody to all complexes using biolayer interferometry (BLI). The nanobody bound  
167 equivalently tightly to all complexes, with ~2 nM potency for p110 $\gamma$ , p110 $\gamma$ -p84, and  
168 p110 $\gamma$ -p101 (Fig. 1B). We also tested binding of the nanobody to all class IA PI3Ks, and  
169 there was no detectable binding to p110 $\alpha$ , p110 $\beta$ , and p110 $\delta$  (Fig. 1C).

170 To further understand the mechanism by which this nanobody blocked lipid  
171 kinase activity we measured the bulk membrane recruitment dynamics of fluorescently  
172 labeled Dy647-p84-p110 $\gamma$  on supported lipid bilayers (SLBs) using Total Internal

173 Reflection Fluorescence (TIRF) Microscopy. We found that the nanobody had no effect  
174 on membrane recruitment of p110 $\gamma$ -p84 on bilayers containing membrane-tethered Ras  
175 (GTP) and G $\beta\gamma$  (Fig. 1D-F). Membrane binding was not affected when the nanobody  
176 was spiked into samples containing membrane associated Dy647-p84-p110 $\gamma$  (Fig 1D).  
177 Similarly, pre-incubation of Dy647-p84-p110 $\gamma$  with 500 nM NB7 did not perturb  
178 membrane association of the kinase when flowed over a supported membrane (Fig.  
179 1E).

180 We wanted to define the molecular mechanism of how nanobody NB7 was a  
181 potent allosteric inhibitor of lipid kinase activity. We purified the complex of nanobody  
182 NB7 bound to p110 $\gamma$ -p84 to homogeneity by gel filtration. Using this sample, we  
183 obtained a cryo-EM reconstruction of the complex of nanobody (NB7)-bound p110 $\gamma$  at  
184 3.0-Å overall resolution from 149,603 particles (Figs. 2A-D, S1-S2 and supplemental  
185 table 1). The density map was of sufficient quality to perform automated and manual  
186 construction of the p110 $\gamma$ -NB7 complex, with unambiguous building of the interfacial  
187 contacts between NB7 and p110 $\gamma$  (Fig. S2). Nanobody binding did not induce any large-  
188 scale conformational changes of p110 $\gamma$ , as the structure of p110 $\gamma$  bound to NB7 was  
189 similar to the apo p110 $\gamma$  crystal structure or p110 $\gamma$ -p101 cryo-EM structure (Fig. S3).  
190 The lowest local resolution was in the ABD domain, with increased B-factors of the ABD  
191 in the p110 $\gamma$ -NB7 structure compared to p110 $\gamma$ -p101 (Fig. S3). This is consistent with  
192 the concept that ABD flexibility plays an important role in class I PI3K regulation (Liu et  
193 al., 2022).

194 The interface between NB7 and p110 $\gamma$  was extensive, with ~1200 Å<sup>2</sup> of buried  
195 surface area, with interactions of the ABD-RBD linker, N-terminus of the helical domain,  
196 and the regulatory motif at the turn between  $\kappa\alpha 8$ - $\kappa\alpha 9$  (1022-1026aa). This location in  
197 the regulatory motif is where both activating oncogenic (R1021C) and inhibitory loss of  
198 function mutants have been identified (R1021P) (Takeda et al., 2019), as well as a  
199 putative inhibitory phosphorylation site (T1024) (Perino et al., 2011). The resolution  
200 was sufficient to unambiguously build the three complementarity determining region  
201 (CDR) loops of NB7 that mediate target selectivity (Fig. 2E-F). The interface is primarily  
202 hydrophobic, with only 8 hydrogen bonds, and 1 electrostatic interaction among the 33

203 interfacial residues of NB7. A pocket formed between the helical domain and the ABD-  
204 RBD linker forms the majority of the interface, with extensive interactions with the long  
205 CDR3. The CDR1 loop packed up against the N-terminal section of the helical domain,  
206 with the CDR2 loop forming the interface with the regulatory motif. Previous study of  
207 oncogenic mutants in the regulatory motif of p110 $\gamma$  showed that increased dynamics  
208 mediated by these mutants increased kinase activity, putatively by breaking the  
209 autoinhibitory tryptophan lock in  $\kappa\alpha 12$  of the regulatory motif (Rathinaswamy et al.,  
210 2021c). Therefore, rigidifying the regulatory motif likely explains the molecular basis for  
211 how it prevents kinase activity. The nanobody interface is distinct from the predicted  
212 G $\beta\gamma$  interface (Rathinaswamy et al., 2023) and the experimentally resolved Ras  
213 interface (Pacold et al., 2000), explaining why it can still be membrane recruited by  
214 these stimuli.

215 The interface of NB7 with p110 $\gamma$  is distant from both the putative membrane  
216 binding surface, as well as the catalytic machinery of the kinase domain. To further  
217 understand how this nanobody could potentially inhibit PI3K activity we examined any  
218 other potential modulators of PI3K activity localised in this region. There are two  
219 regulatory phosphorylation sites in the helical (Walser et al., 2013) and kinase domain  
220 (Perino et al., 2011) localised at the NB7 interface. This is intriguing as helical domain  
221 phosphorylation is activating, and kinase domain phosphorylation is inhibitory. This  
222 suggested a critical role in the regulation of p110 $\gamma$  is the dynamics of this kinase-helical  
223 interface. To fully define the role of NB7 in altering the dynamics of the helical domain  
224 we needed to study other modulators of helical domain dynamics.

225

### 226 *p110 $\gamma$ activation by helical domain phosphorylation*

227 To further understand the potential role of helical domain dynamics in controlling  
228 p110 $\gamma$  activity we examined the role of S582 helical domain phosphorylation by the  
229 protein kinase PKC $\beta$ II (encoded by the gene *PRKCB2*, referred to as PKC $\beta$  for  
230 simplicity throughout the manuscript) (Walser et al., 2013). S582 is located on the  
231 interior of the helical domain and would not be expected to be exposed when the N-  
232 terminal region of the helical domain is folded (Fig. 3A). To understand this better at a  
233 molecular level, we purified a catalytic fragment of PKC $\beta$  and performed protein

234 phosphorylation reactions on p110 $\gamma$  apo, p110 $\gamma$ -p84, and p110 $\gamma$ -p101. We identified a  
235 phosphorylated peptide containing S582, and surprisingly, we found an additional p110 $\gamma$   
236 phosphorylation site at either S594/S595 (Fig. 3B, Fig. S4). The modification at this site  
237 results in a single phosphorylation event, but due to CID MS/MS fragmentation we  
238 cannot determine which site is modified, and we will refer it as S594/S595 throughout  
239 the manuscript. The S594/S595 site is also located in the N-terminal region of the  
240 helical domain, and is even more buried than S582, and would not be expected to be  
241 exposed when this region is folded (Fig. 3A). Dose response curves of PKC $\beta$  treatment  
242 was carried out for p110 $\gamma$  (Fig. 3C), p110 $\gamma$ -p84 (Fig. 3D), and p110 $\gamma$ -p101 (Fig. 3E).  
243 Both p110 $\gamma$  and p110 $\gamma$ -p84 showed similar dose response curves for PKC $\beta$  treatment,  
244 with similar curves for S582 and S594/S595. The p110 $\gamma$ -p101 complex was only very  
245 weakly phosphorylated, with <100-fold lower levels compared to p110 $\gamma$  and p110 $\gamma$ -p84  
246 (Fig. 3E). This is consistent with the helical domain in p110 $\gamma$  being more rigid when  
247 bound to p101, compared to either bound to p84 or p110 $\gamma$  alone.

248 To provide additional insight into the molecular mechanisms underlying p110 $\gamma$   
249 phosphorylation we carried out hydrogen deuterium exchange mass spectrometry  
250 (HDX-MS) experiments on p110 $\gamma$  and phosphorylated p110 $\gamma$  (90.8% phosphorylated  
251 S594/595, 92% phosphorylated S582) (Fig. 4A). The full data underlying the experiment  
252 is available in the source data, and data processing information is in supplemental table  
253 2. We have previously observed that the N-terminal region of the helical domain of apo  
254 p110 $\gamma$  (residues spanning 557-630aa) shows isotope profiles that are consistent with  
255 EX1 H/D exchange kinetics (Rathinaswamy et al., 2021b, 2021c; Vadas et al., 2013;  
256 Walser et al., 2013). This is indicative of cooperative unfolding of extended protein  
257 regions, with H/D exchange occurring faster than the refolding event. This region is  
258 where the PKC $\beta$  phosphorylation sites are located and may explain how the buried  
259 residues S582 and S594/S595 can be exposed to PKC $\beta$ . This is compatible with the  
260 observation that p110 $\gamma$ -p101 is protected from phosphorylation, as it does not show EX1  
261 kinetics in this region, whereas both p110 $\gamma$  and p110 $\gamma$ -p84 do (Rathinaswamy et al.,  
262 2021a).

263           When we compared phosphorylated p110 $\gamma$  (>90.8% as measured by mass  
264 spectrometry at both sites) to unphosphorylated p110 $\gamma$  we observed extensive  
265 increases in dynamics in the C2, helical domain and kinase domain (Fig. 4A-D). The  
266 largest increases in exchange upon phosphorylation were located in the N-terminal  
267 region of the helical domain, with the peptides directly adjacent to the phosphorylation  
268 site showing almost complete deuterium incorporation at the earliest time points of  
269 exchange. This is indicative of significant disruption of the alpha helical secondary  
270 structure in this region. When we examined the exchange profiles in this region, they  
271 still underwent EX1 kinetics (Fig. 4C), however, phosphorylated p110 $\gamma$  was enriched in  
272 the more fully deuterated species. In addition to the regions in the helical domain, a  
273 portion of the regulatory motif of the kinase domain also showed increased deuterium  
274 exposure. This included the  $\kappa\alpha 9$ - $\kappa\alpha 12$  helices that surround the activation loop of p110 $\gamma$ .  
275 These increases in exchange were similar to those we had observed in a R1021C  
276 oncogenic activating mutant of *PIK3CG* (Rathinaswamy et al., 2021c).

277           To further explore the potential role of phosphorylation in mediating p110 $\gamma$   
278 activity, we examined the kinase activity of p110 $\gamma$  under two conditions: basal ATP  
279 turnover, and with PIP<sub>2</sub> containing lipid membranes. The experiments in the absence of  
280 PIP<sub>2</sub> measure turnover of ATP into ADP and phosphate and is a readout of basal  
281 catalytic competency. Experiments with PIP<sub>2</sub>, measured ATP consumed in the  
282 generation of PIP<sub>3</sub>, as well as in non-productive ATP turnover. The p110 $\gamma$  enzyme in the  
283 absence of stimulators is very weakly active towards PIP<sub>2</sub> substrate with only ~2 fold  
284 increased ATP turnover compared to in the absence of membranes. This is consistent  
285 with very weak membrane recruitment of p110 $\gamma$  complexes in the absence of lipid  
286 activators (Rathinaswamy et al., 2023). PKC $\beta$ -mediated phosphorylation enhanced the  
287 ATPase activity of p110 $\gamma$  ~2-fold in both the absence and presence of membranes (Fig.  
288 4E). This suggests that the effect of phosphorylation is to change the intrinsic catalytic  
289 efficiency of phosphorylated p110 $\gamma$ , with limited effect on membrane binding.

290

291 *Nanobody decreases p110 $\gamma$  phosphorylation*



292 As NB7 bound at the interface of the helical and kinase domains that is exposed  
293 upon PKC $\beta$  phosphorylation of p110 $\gamma$  we hypothesized that the nanobody would likely  
294 alter phosphorylation. We carried out PKC $\beta$  phosphorylation of p110 $\gamma$ , p110 $\gamma$ -p101 and  
295 p110 $\gamma$  bound to NB7. The presence of NB7 showed a significant decrease in p110 $\gamma$   
296 phosphorylation at both sites (Fig. 5A-B). We also wanted to determine whether p110 $\gamma$   
297 phosphorylation reciprocally perturbed NB7 binding. BLI experiments showed that there  
298 was no detectable binding of NB7 to phosphorylated p110 $\gamma$  (Fig. 5C-D), consistent with  
299 phosphorylation disrupting the N-terminal region of the p110 $\gamma$  helical domain. In  
300 addition, lipid kinase assays using phosphorylated p110 $\gamma$  showed no detectable  
301 difference in activity when measured in the absence and presence nanobody (Fig. 5E),  
302 consistent with NB7 being unable to bind to phosphorylated p110 $\gamma$ .

303

## 304 Discussion

305 Here we find that the helical domain is a central regulator of the p110 $\gamma$  catalytic  
306 subunit of class IB PI3K, with modulation of helical dynamics through binding partners  
307 or PTMs able to either increase or decrease lipid kinase activity. These results expand  
308 on previous work defining the helical domain as a central regulator of class IA PI3Ks,  
309 where the nSH2 domain of the p85 regulatory subunits makes inhibitory interactions  
310 that significantly inhibit lipid kinase activity of all class IA catalytic subunits (p110 $\alpha$ ,  
311 p110 $\beta$ , and p110 $\delta$ ) (Mandelker et al., 2009; Miled et al., 2007; Burke and Williams,  
312 2013; Burke, 2018). This inhibitory interaction in class IA PI3Ks is disrupted in human  
313 cancers (helical hotspot mutations in *PIK3CA*) (Samuels et al., 2004) and immune  
314 disorders (helical mutations in *PIK3CD* in APDS1) (Angulo et al., 2013; Lucas et al.,  
315 2014). Class IB PI3Ks are unique compared to class IA PI3Ks, as they are not inhibited  
316 by p101 and p84 regulatory subunits, but instead potentiate GPCR activation. This lack  
317 of inhibition is due to the distinct binding interface of class IB PI3K regulatory subunits  
318 compared to class IA regulatory subunits, with only class IA regulatory subunits making  
319 direct inhibitory interactions with the kinase and helical domains of p110 catalytic  
320 subunits (Rathinaswamy et al., 2021a). Here we show that a unique surface at the



321 interface of the helical and kinase domains of p110 $\gamma$  is a potential site for the  
322 development of novel allosteric inhibitors that modulate p110 $\gamma$  activity.

323 The previously identified inhibitory nanobody (NB7) (Rathinaswamy et al., 2021b)  
324 bound with high affinity and inhibited all complexes of p110 $\gamma$ . The nanobody interface is  
325 distinct from how the nSH2 inhibits class IA PI3K activity, as its binding site is on the  
326 opposite face of the helical domain (Fig. 6A). The mechanism of inhibition is also  
327 distinct, as the nSH2-helical interaction plays a critical role in preventing membrane  
328 recruitment of inhibited class I PI3Ks, with removal of this interface either through  
329 pYXXM motif binding, or oncogenic mutations leading to increased membrane  
330 recruitment (Burke et al., 2012, 2011; Zhang et al., 2011). Analysis of the nanobody  
331 binding site compared to the structure of HRas-p110 $\gamma$  or the HDX-MS supported  
332 AlphaFold-multimer prediction of G $\beta$  $\gamma$ -p110 $\gamma$  (Rathinaswamy et al., 2023) shows that  
333 nanobody binding does not sterically block complex formation (Fig. 6B). This is  
334 consistent with it not blocking membrane recruitment by Ras/G $\beta$  $\gamma$ . The nanobody  
335 inhibited ATP turnover both in solution and on membranes, suggesting that it prevents  
336 formation of a catalytically competent conformation of p110 $\gamma$ , but still allows for  
337 membrane recruitment. Further development of small molecule allosteric binding  
338 partners in this allosteric pocket between the kinase and helical domain may reveal the  
339 specific molecular interactions in this pocket that mediate inhibition.

340 Oncogenic mutations are frequent in the class IA PI3K $\alpha$  encoded by *PIK3CA*,  
341 with this being the 2<sup>nd</sup> most frequently mutated gene in human cancer (Lawrence et al.,  
342 2014). Mutations in p110 $\gamma$  encoded by *PIK3CG* in cancer are less frequent, however,  
343 they can still provide insight into regulatory mechanisms that control activity. Oncogenic  
344 mutations in the kinase domain (R1021C) and helical domain (E581K) are in close  
345 proximity to the nanobody binding site, and both would be expected to disrupt the  
346 stability of the helical domain or regulatory motif of the kinase domain (Fig. 6C). In  
347 addition to these mutations there are also multiple post-translational modifications that  
348 occur in this region, including inhibitory phosphorylation at T1024 (Perino et al., 2011),  
349 and activating phosphorylation at S582 (Walser et al., 2013). PKC $\beta$  is activated  
350 downstream of the IgE receptor in mast cells (Walser et al., 2013), but the full details of

351 how this activates PI3K has been unclear. We identified an additional PKC $\beta$   
352 phosphorylation site located in the helical domain (S594/S595) (Fig. 6C). Both the S582  
353 and S594/S595 sites are not surface accessible and would require a transient opening  
354 of the helical domain for kinase accessibility. HDX-MS analysis of the helical domain of  
355 p110 $\gamma$  has shown that it is more dynamic than other class I PI3K isoforms (Burke and  
356 Williams, 2013; Walser et al., 2013), with the presence of the p101 regulatory subunit  
357 dramatically decreasing helical domain dynamics (Vadas et al., 2013). This putative  
358 mechanism of helical domain dynamics driving PKC $\beta$  phosphorylation is consistent with  
359 our observation that p101 subunits decreased p110 $\gamma$  phosphorylation >100-fold. PKC $\beta$   
360 phosphorylation of p110 $\gamma$  leads to increased dynamics in both the helical and kinase  
361 domains with increased kinase activity, although only weakly compared to full activation  
362 by either membrane localised Ras or G $\beta\gamma$ . This increase was observed with both  
363 membrane and soluble substrate, so likely is not driven by altered membrane  
364 recruitment.

365 Overall, our biophysical and biochemical analysis of modulators of helical domain  
366 dynamics reveal the critical role of this domain in regulating class IB PI3K activity. This  
367 raises possibilities for development of small molecule modulators that may either  
368 increase or decrease helical domain dynamics, leading to either activation or inhibition.  
369 The high-resolution structure of an allosteric inhibitor nanobody provide initial insight  
370 into which pockets can specifically be targeted. Multiple ATP competitive p110 $\gamma$   
371 selective inhibitors are in clinical trials for human cancers (Li et al., 2021), with many  
372 having significant side effects. The identification of novel inhibitory strategies provides  
373 new opportunities for targeting p110 $\gamma$  dysregulation in human disease.

374

### 375 **Acknowledgements**

376 J.E.B. is supported by the Canadian Institute of Health Research (CIHR,  
377 168998), and the Michael Smith Foundation for Health Research (MSFHR, scholar  
378 17686). C.K.Y. is supported by CIHR (FDN-143228, PJT-168907) and the Natural  
379 Sciences and Engineering Research Council of Canada (RGPIN-2018-03951). S.D.H. is  
380 supported by an NSF CAREER Award (MCB-2048060). This research project was  
381 supported in part by the UBC High Resolution Macromolecular Cryo-Electron

382 Microscopy Facility (HRMEM). A portion of this research was supported by NIH grant  
 383 U24GM129547 and performed at the PNCC at OHSU and accessed through EMSL  
 384 (grid.436923.9), a DOE Office of Science User Facility sponsored by the Office of  
 385 Biological and Environmental Research. We appreciate help from Theo Humphreys and  
 386 Rose Marie Haynes with data collection at PNCC. Competing Interests: The authors  
 387 declare that they have no competing interests.

388

### 389 **Conflict of Interest statement**

390 JEB reports personal fees from Scorpion Therapeutics, Reactive therapeutics  
 391 and Olema Oncology; and research grants from Novartis. Other authors declare no  
 392 competing interests.

393

### 394 **Methods**

<b>Resources table</b>	SOURCE	IDENTIFIER
<b>Bacterial and virus strains</b>		
E.coli XL10-GOLD KanR Ultracompetent Cells	Agilent	200317
E.coli DH10EMBacY Competent Cells	Geneva Biotech	DH10EMBacY
<b>Chemicals, peptides, and recombinant proteins</b>		
Deuterium Oxide 99.9%	Sigma	151882
Guanosine 5'-diphosphate (GDP) sodium salt hydrate	Sigma	G7127-100MG
Guanosine 5'-triphosphate (GTP) sodium salt hydrate	Sigma	G8877-250MG
Sodium deoxycholate	Sigma	D6750
Polyoxyethylene (10) lauryl ether	Sigma	P9769
CHAPS, Molecular Biology Grade	EMD Millipore	220201
Phosphatidylserine (Porcine Brain)	Avanti	840032C
Phosphatidylethanolamine (Egg yolk)	Sigma	P6386
Cholesterol	Sigma	47127-U
Phosphatidylcholine (Egg yolk)	Avanti	840051C
Phosphatidylinositol-4,5-bisphosphate (Porcine Brain)	Avanti	840046
Sphingomyelin (Egg yolk)	Sigma	S0756
1,2-dioleoyl-sn-glycero-3-phosphocholine (DOPC)	Avanti	850375C
1,2-dioleoyl-sn-glycero-3-phospho-L-serine (18:1, DOPS)	Avanti	840035C
1,2-dioleoyl-sn-glycero-3-phosphoethanolamine-N-[4-(p-maleimidomethyl)cyclohexane-carboxamide] (18:1 MCC-PE)	Avanti	780201C
10 mg/mL beta casein solution	ThermoFisher	37528
10x PBS [pH 7.4]	Corning	46-013-CM
glucose oxidase from <i>Aspergillus niger</i> (225 U/mg)	Biophoretics	B01357.02
catalase	Sigma	C40-100MG Bovine Liver
Trolox	Cayman	10011659

	Chemicals	
Dyomics 647 maleimide dye	Dyomics	647P1-03
Coenzyme A	Sigma	C3019
Sulfuric acid	Sigma	58105-2.5L-PC
<b>Critical commercial assays</b>		
Transcriber ADP2 FI Assay (1,000 Assay, 384 Well)	BellBrook Labs	3013-1K
<b>Deposited data</b>		
PDB coordinate file for p110 $\gamma$ -NB7 structure	PDB	8DP0
EM density file for p110 $\gamma$ -NB7 complex	EMD	EMD-27627
HDX-MS and phosphorylation proteomics data	PRIDE	PXD040765
<b>Oligonucleotides</b>		
Fwd primer for amplifying KD of PKC $\beta$ II GTATTTTCAGGGCgcccgtaccACGACCAACTGTCT CCAAATTTG	Sigma	MR51F
Rvs primer for amplifying KD of PKC $\beta$ II gactcgagcggccgcTTATAGCTCTTGACTTCGGGTTTTA AAAATTCAG	Sigma	MR51R
Fwd primer for amplifying N term of PKC $\beta$ II CCATCACggatctggcggtagtATGGCTGACCCGGCTGCG	Sigma	MR52F
Rvs primer for amplifying N term of PKC $\beta$ II GCCCTGAAAATACAGGTTTTCTTTCTTCCGGGAC CTTGGTTCCC	Sigma	MR52R
Fwd primer for adding stop codon to PKC $\beta$ II AGTCAAGAGCTAAgcccggcctcgagtctagagcctgc	Sigma	MR56F
Rvs primer for adding stop codon to PKC $\beta$ II gactcgagcggccgcTTAGCTCTTGACTTCGGGTTTTAAA AATTCAG	Sigma	MR56R
<b>Recombinant DNA</b>		
pMultiBac-G $\beta$ 1/G $\gamma$ 2	PMID:34452907	pOP737
pACEBac1-hsp110 $\gamma$	PMID:34452907	MR30
pMultiBac-hsp110 $\gamma$ -ssp101	PMID:34452907	MR22
pMultiBac-hsp110 $\gamma$ -mmp84	PMID:34452907	MR24
pFastBac HRas G12V	PMID:34452907	BS9
biGBac hsp110 $\gamma$ /ybbr-hsp84	PMID:36842083	HP28
biGBac hsp110 $\gamma$ /ybbr-hsp101	PMID:36842083	HP29
his6-GST-PrescissionProtease-SNAP-RBD(K65E)	PMID:34452907	pSH936
his6TEV-HRas(1-184aa) C118S, C181S	PMID:34452907	pSH414
his6-G $\gamma$ 2, SNAP-G $\beta$ 1 (DUAL FastBac)	PMID:34452907	pSH651
pACEBAC-PKC $\beta$ II (internal tev cleavage site)	This paper	pMR56
pFASTBac p110 $\alpha$	PMID: 28515318	pOV1181
pFASTBac p110 $\beta$	PMID: 28515318	pOV1182
pFASTBac p110 $\delta$	PMID: 28515318	pOV1183
pFASTBac p85 $\beta$	This paper	EX21
<b>Software and algorithms</b>		
COOT-0.9.4.1	CCP4	<a href="https://www2.mrc-lmb.cam.ac.uk/personal/pemsley/coot/">https://www2.mrc-lmb.cam.ac.uk/personal/pemsley/coot/</a>

Phenix-1.19.1	Open source	<a href="https://www.phenix-online.org/">https://www.phenix-online.org/</a>
PDBePISA (Proteins, Interfaces, Structures and Assemblies)	EMBL-EBI	<a href="https://www.ebi.ac.uk/pdbe/pisa/pistart.html">https://www.ebi.ac.uk/pdbe/pisa/pistart.html</a>
ESPrIPT 3.0	Robert et al NAR 2014	<a href="https://espript.ibcp.fr">https://espript.ibcp.fr</a>
HDExaminer	Sierra Analytics	<a href="http://massspec.com/hdexaminer">http://massspec.com/hdexaminer</a>
GraphPad Prism 7	GraphPad	<a href="https://www.graphpad.com">https://www.graphpad.com</a>
PyMOL	Schroedinger	<a href="http://pymol.org">http://pymol.org</a>
Compass Data Analysis	Bruker	<a href="https://www.bruker.com">https://www.bruker.com</a>
ChimeraX	UCSF	<a href="https://www.rbvi.ucsf.edu/chimera/">https://www.rbvi.ucsf.edu/chimera/</a>
ImageJ/Fiji	ImageJ	<a href="https://imagej.net/software/fiji/">https://imagej.net/software/fiji/</a>
Nikon NIS elements	Nikon	<a href="https://www.microscope.healthcare.nikon.com/products/software/nis-elements">https://www.microscope.healthcare.nikon.com/products/software/nis-elements</a>
cryoSPARC v.3.3.2	Structura Biotechnology	<a href="https://cryosparc.com/">https://cryosparc.com/</a>
<b>Other</b>		
Sf9 insect cells for expression	Expression Systems	94-001S
Insect cell media	Expression Systems	96-001-01
Hellmanex III cleaning solution	Fisher	14-385-864
6-well sticky-side chamber	IBIDI	80608
C-Flat 2/2-T grids	Electron Microscopy Sciences	CFT-223C

395

396

### 397 *Plasmid Generation*

398 Plasmids encoding Homo sapiens p110 $\gamma$  (human), Mus musculus p84 (mouse), Sus  
399 scrofa p101 (porcine), and G $\beta\gamma$  were used as previously described (Rathinaswamy et  
400 al., 2023, 2021a). The plasmids encoding the class IA PI3Ks were also used as  
401 previously described (Dornan et al., 2017; Siempelkamp et al., 2017). The pDONR223-  
402 PRKCB2 (PKC $\beta$ II, uniprot identifier: P05771-2) was a gift from William Hahn & David  
403 Root (Addgene plasmid #23746; [http://n2t.net/addgene: 23746](http://n2t.net/addgene:23746); RRID:Addgene\_23746)  
404 (Johannessen et al., 2010). The PKC $\beta$ II construct contains an internal TEV site that  
405 cleaves the catalytic domains from the C1/C2 regulatory domains (TEV site inserted  
406 between residues 320 and 321 of PKC $\beta$ ). This construct was subcloned into a  
407 pACEBAC Sf9 expression vector for Sf9 protein production. All constructs were cloned

408 to include a 10× histidine tag, a 2× strep tag, and a tobacco etch virus protease  
409 cleavage site on the N terminus. For p110γ and PKCβII this tag was included at the N-  
410 terminus, with this tag included at the N-terminus of either p84 or p101 for purification of  
411 p110γ-p101 and p110γ-p84. Full details of the plasmids are included in the resource  
412 table.

413

#### 414 *Virus Generation and Amplification:*

415 The plasmids encoding genes for insect cell expression were transformed into  
416 DH10MultiBac cells (MultiBac, Geneva Biotech) to generate bacmid containing the  
417 genes of interest. Successful generation was identified by blue-white colony screening  
418 and the bacmid was purified using a standard isopropanol-ethanol extraction method.  
419 Bacteria were grown overnight (16 hours) in 3-5 mL 2xYT (BioBasic #SD7019). Cells  
420 were spun down and the pellet was resuspended in 300 μL of 50 mM Tris-HCl, pH 8.0,  
421 10 mM EDTA, 100 mg/mL RNase A. The pellet was lysed by the addition of 300 μL of  
422 1% sodium dodecyl sulfate (SDS) (W/V), 200 mM NaOH, and the reaction was  
423 neutralized by addition of 400 μL of 3.0 M potassium acetate, pH 5.5. Following  
424 centrifugation at 21130 RCF and 4 °C (Rotor #5424 R), the supernatant was mixed with  
425 800 μL isopropanol to precipitate bacmid DNA. Following centrifugation, the pelleted  
426 bacmid DNA was washed with 500 μL 70% Ethanol three times. The pellet was then air  
427 dried for 1 minute and re-suspended in 50 μL Buffer EB (10 mM Tris-Cl, pH 8.5; All  
428 buffers from QIAprep Spin Miniprep Kit, Qiagen #27104). Purified bacmid was then  
429 transfected into Sf9 cells. 2 mL of Sf9 cells at 0.6X10<sup>6</sup> cells/mL were aliquoted into a 6-  
430 well plate and allowed to attach to form a confluent layer. Transfection reactions were  
431 prepared mixing 8-12 μg of bacmid DNA in 100 μL 1xPBS and 12 μg polyethyleneimine  
432 (Polyethyleneimine “Max” MW 40.000, Polysciences #24765, USA) in 100 μL 1xPBS  
433 and the reaction was allowed to proceed for 20-30 minutes before addition to an Sf9  
434 monolayer containing well. Transfections were allowed to proceed for 5-6 days before  
435 harvesting virus containing supernatant as a P1 viral stock.

436 Viral stocks were further amplified by adding P1 to Sf9 cells at ~2x10<sup>6</sup> cells/mL  
437 (2/100 volume ratio). This amplification was allowed to proceed for 4-5 days and  
438 resulted in a P2 stage viral stock that was used in final protein expression. Harvesting of



439 P2 viral stocks was carried out by centrifuging cell suspensions in 50 mL Falcon tubes  
440 at 2281 RCF (Beckman GS-15). To the supernatant containing virus, 5-10% inactivated  
441 fetal bovine serum (FBS; VWR Canada #97068-085) was added and the stock was  
442 stored at 4°C.

443  
444 *Expression and purification of PI3K $\gamma$ , PI3K $\alpha/\beta/\delta$  and PKC $\beta$  constructs:*  
445 PI3K $\gamma$  and PKC $\beta$  constructs were expressed in Sf9 insect cells using the baculovirus  
446 expression system. Following 55 hours after infection with P2 viral stocks, cells were  
447 harvested by centrifuging at 1680 RCF (Eppendorf Centrifuge 5810 R) and the pellets  
448 were snap-frozen in liquid nitrogen. The complex was purified through a combination of  
449 nickel affinity, streptavidin affinity and size exclusion chromatography.

450 Frozen insect cell pellets were resuspended in lysis buffer (20 mM Tris pH 8.0,  
451 100 mM NaCl, 10 mM imidazole pH 8.0, 5% glycerol (v/v), 2 mM  $\beta$ ME), protease  
452 inhibitor (Protease Inhibitor Cocktail Set III, Sigma)) and sonicated for 2 minutes (15s  
453 on, 15s off, level 4.0, Misonix sonicator 3000). Triton-X was added to the lysate to a  
454 final concentration of 0.1% and clarified by spinning at 15,000 RCF at 4°C for 45  
455 minutes (Beckman Coulter JA-20 rotor). The supernatant was loaded onto a 5 mL  
456 HisTrap™ FF crude column (GE Healthcare) equilibrated in NiNTA A buffer (20 mM Tris  
457 pH 8.0, 100 mM NaCl, 20 mM imidazole pH 8.0, 5% (v/v) glycerol, 2 mM  $\beta$ ME). The  
458 column was washed with high salt NiNTA A buffer (20 mM Tris pH 8.0, 1 M NaCl, 20  
459 mM imidazole pH 8.0, 5% (v/v) glycerol, 2 mM  $\beta$ ME), NiNTA A buffer, 6% NiNTA B  
460 buffer (20 mM Tris pH 8.0, 100 mM NaCl, 250 mM imidazole pH 8.0, 5% (v/v) glycerol,  
461 2 mM  $\beta$ ME) and the protein was eluted with 100% NiNTA B. The eluent was loaded  
462 onto a 5 mL StrepTrap™ HP column (GE Healthcare) equilibrated in gel filtration buffer  
463 (20mM Tris pH 8.5, 100 mM NaCl, 50 mM Ammonium Sulfate and 0.5 mM TCEP). To  
464 purify PI3K $\alpha/\beta/\delta$ , the purification protocol was performed as described above but  
465 instead the protein was eluted in PI3K $\alpha$  gel filtration buffer (20mM HEPES 7.5, 150mM  
466 NaCl, 0.5mM TCEP). The column was washed with the corresponding gel filtration  
467 buffer and loaded with tobacco etch virus protease. After cleavage on the column  
468 overnight, the PI3K $\gamma$  protein constructs were eluted in gel filtration buffer. The protein  
469 was concentrated in a 50,000 MWCO Amicon Concentrator (Millipore) to <1 mL and



470 injected onto a Superdex™ 200 10/300 GL Increase size-exclusion column (GE  
471 Healthcare) equilibrated in gel filtration buffer. After size exclusion, the protein was  
472 concentrated, aliquoted, frozen, and stored at -80°C. For PKCβ, the protein was eluted  
473 from the strep column in gel filtration buffer, and the eluate was then loaded on a 1ml  
474 HisTrap™ FF column to remove his tagged LipTev. The flowthrough was collected, and  
475 the column was washed with 2ml of gel filtration buffer. These fractions were pooled  
476 and concentrated and stored at -80°C.

477 To purify phosphorylated p110γ, the purification protocol as described above was  
478 performed but PKCβ was added to the strep column at a molar ratio of 1:3  
479 (PKCβ:p110γ) along with LipTEV, 20 mM MgCl<sub>2</sub> and 1mM ATP and allowed to incubate  
480 on ice for 4 hours. The protein was eluted by adding 7 ml of gel filtration buffer and  
481 treated with a second dose of PKCβ (same ratio as above) and allowed to incubate on  
482 ice for another 3 hours. For non-phosphorylated p110γ, same protocol was followed with  
483 the exception in the addition of PKCβ. Both the proteins were concentrated in a 50,000  
484 MWCO Amicon Concentrator (Millipore) to <1 mL and injected onto a Superdex™ 200  
485 10/300 GL Increase size-exclusion column (GE Healthcare) equilibrated in gel filtration  
486 buffer. The final phosphorylation level of the two sites was characterised by mass  
487 spectrometry, with these values being 92% and 90.8%, for S582 and S594/S595  
488 respectively. After size exclusion, the protein was concentrated, aliquoted, frozen, and  
489 stored at -80°C.

490

#### 491 *Expression and Purification of lipidated Gβγ for kinase activity assays:*

492 Full length, lipidated human Gβγ (Gβ1γ2) was expressed in Sf9 insect cells and  
493 purified as described previously. After 65 hours of expression, cells were harvested, and  
494 the pellets were frozen as described above. Pellets were resuspended in lysis buffer (20  
495 mM HEPES pH 7.7, 100 mM NaCl, 10 mM βME, protease inhibitor (Protease Inhibitor  
496 Cocktail Set III, Sigma)) and sonicated for 2 minutes (15s on, 15s off, level 4.0, Misonix  
497 sonicator 3000). The lysate was spun at 500 RCF (Eppendorf Centrifuge 5810 R) to  
498 remove intact cells and the supernatant was centrifuged again at 25,000 RCF for 1 hour  
499 (Beckman Coulter JA-20 rotor). The pellet was resuspended in lysis buffer and sodium  
500 cholate was added to a final concentration of 1% and stirred at 4°C for 1 hour. The

501 membrane extract was clarified by spinning at 10,000 RCF for 30 minutes (Beckman  
502 Coulter JA-20 rotor). The supernatant was diluted 3 times with NiNTA A buffer (20 mM  
503 HEPES pH 7.7, 100 mM NaCl, 10 mM Imidazole, 0.1% C12E10, 10mM  $\beta$ ME) and  
504 loaded onto a 5 mL HisTrap™ FF crude column (GE Healthcare) equilibrated in the  
505 same buffer. The column was washed with NiNTA A, 6% NiNTA B buffer (20 mM  
506 HEPES pH 7.7, 25 mM NaCl, 250 mM imidazole pH 8.0, 0.1% C12E10, 10 mM  $\beta$ ME)  
507 and the protein was eluted with 100% NiNTA B. The eluent was loaded onto HiTrap™ Q  
508 HP anion exchange column equilibrated in Hep A buffer (20 mM Tris pH 8.0, 8 mM  
509 CHAPS, 2 mM Dithiothreitol (DTT)). A gradient was started with Hep B buffer (20 mM  
510 Tris pH 8.0, 500 mM NaCl, 8 mM CHAPS, 2 mM DTT) and the protein was eluted in  
511 ~50% Hep B buffer. The eluent was concentrated in a 30,000 MWCO Amicon  
512 Concentrator (Millipore) to < 1 mL and injected onto a Superdex™ 75 10/300 GL size  
513 exclusion column (GE Healthcare) equilibrated in Gel Filtration buffer (20 mM HEPES  
514 pH 7.7, 100 mM NaCl, 10 mM CHAPS, 2 mM TCEP). Fractions containing protein were  
515 pooled, concentrated, aliquoted, frozen and stored at -80 °C.

516

#### 517 *Expression and purification of nanobody:*

518 Nanobody NB7-PIK3CG with a C-terminal 6X His tag was expressed from a  
519 pMESy4 vector in the periplasm of WK6 *E. coli*. A 1L culture was grown to OD600 of 0.7  
520 in Terrific Broth containing 0.1% glucose and 2mM MgCl<sub>2</sub> in the presence of 100  $\mu$ g/mL  
521 ampicillin and was induced with 0.5 mM isopropyl- $\beta$ -D-thiogalactoside (IPTG). Cells  
522 were harvested the following day by centrifuging at 2500 RCF (Eppendorf Centrifuge  
523 5810 R) and the pellet was snap-frozen in liquid nitrogen. The frozen pellet was  
524 resuspended in 15 mL of TES buffer containing 200 mM Tris pH 8.0, 0.5mM  
525 ethylenediaminetetraacetic acid (EDTA) and 500 mM Sucrose and was mixed for 45  
526 minutes at 4°C. To this mixture, 30 mL of TES buffer diluted four times in water was  
527 added and mixed for 45 minutes at 4°C to induce osmotic shock. The lysate was  
528 clarified by centrifuging at 14,000 rpm for 15 minutes (Beckman Coulter JA-20 rotor).  
529 Imidazole was added to the supernatant to final concentration of 10mM loaded onto a 5  
530 mL HisTrap™ FF crude column (GE Healthcare) equilibrated in NiNTA A buffer (20 mM  
531 Tris pH 8.0, 100 mM NaCl, 20 mM imidazole pH 8.0, 5% (v/v) glycerol, 2 mM  $\beta$ -

532 mercaptoethanol ( $\beta$ ME)). The column was washed with high salt NiNTA A buffer (20  
533 mM Tris pH 8.0, 1 M NaCl, 20 mM imidazole pH 8.0, 5% (v/v) glycerol, 2 mM  $\beta$ ME),  
534 followed by 100% NiNTA A buffer, then a 6% NiNTA B wash buffer (20 mM Tris pH 8.0,  
535 100 mM NaCl, 250 mM imidazole pH 8.0, 5% (v/v) glycerol, 2 mM  $\beta$ ME) and the protein  
536 was eluted with 100% NiNTA B. The eluent was concentrated in a 10,000 MWCO  
537 Amicon Concentrator (Millipore) to <1 mL and injected onto a Superdex™ 75 10/300 GL  
538 Increase size-exclusion column (GE Healthcare) equilibrated in gel filtration buffer  
539 (20mM Tris pH 8.5, 100 mM NaCl, 50 mM Ammonium Sulfate and 0.5 mM tris(2-  
540 carboxyethyl) phosphine (TCEP)). Following size exclusion, the protein was  
541 concentrated, frozen and stored at  $-80^{\circ}\text{C}$ .

542

#### 543 *Lipid vesicle preparation for kinase activity assays*

544 Lipid vesicles containing 5% brain phosphatidylinositol 4,5- bisphosphate (PIP<sub>2</sub>),  
545 and 95% brain phosphatidylserine (PS), were prepared by mixing the lipids solutions in  
546 organic solvent. The solvent was evaporated in a stream of argon following which the  
547 lipid film was desiccated in a vacuum for 45 minutes. The lipids were resuspended in  
548 lipid buffer (20 mM HEPES pH 7.0, 100 mM NaCl and 10 % glycerol) and the solution  
549 was vortexed for 5 minutes followed by sonication for 15 minutes. The vesicles were  
550 then subjected to ten freeze thaw cycles and extruded 11 times through a 100-nm filter  
551 (T&T Scientific: TT-002-0010). The extruded vesicles were sub-aliquoted and stored at -  
552  $80^{\circ}\text{C}$ . Final vesicle concentration was 2 mg/mL.

553

#### 554 *Kinase Assays*

555 All kinase assays were done using Transcreener ADP2 Fluorescence Intensity  
556 (FI) assays (Bellbrook labs) which measures ADP production. All assays contained ATP  
557 at a final concentration of 100  $\mu\text{M}$ , and those with membranes used vesicles containing  
558 5% phosphatidylinositol 4,5-bisphosphate (PI(4,5)P<sub>2</sub>), and 95% phosphatidylserine (PS)  
559 at a final concentration of 0.5 mg/mL.

560 For assays measuring the inhibition by nanobody, 4X kinase (final concentration:  
561 330 nM for p110 $\gamma$ , 300nM for p110 $\gamma$ /p84 and 12nM for p110 $\gamma$ /p101) was mixed with  
562 varying 4X concentrations of nanobody (final concentration: 2 $\mu\text{M}$  – 2.7nM) or kinase

563 buffer (20mM HEPES pH 7.5, 100mM NaCl, 3mM MgCl<sub>2</sub>, 0.03% CHAPS, 2mM TCEP,  
564 and 1mM EGTA) and allowed to sit on ice for 15 minutes. 2 µl of protein mix was mixed  
565 with 2 µl of lipid solution containing Gβγ (1µM final concentration), ATP (100 µM), PIP<sub>2</sub>  
566 lipid vesicles (0.5mg/ml final concentration), and lipid buffer (25mM HEPES pH 7, 5%  
567 Glycerol, and 100mM NaCl) and incubated at 20°C for 60 minutes.

568 For assays comparing the difference in activation between phosphorylated and  
569 non-phosphorylated p110γ, 2X kinase (final concentrations: 1µM) was mixed with 2X  
570 lipid solutions containing ATP (100 µM), and lipid buffer and either nanobody (3 µM final  
571 concentration), PIP<sub>2</sub> lipid vesicles (0.5mg/ml final concentration) or both nanobody and  
572 lipid. The reaction was incubated at 20°C for 60 minutes.

573 After the 60-minute incubation, all reactions were stopped with 4 µL of 2X stop  
574 and detect solution containing Stop and Detect buffer (20mM HEPES, 0.02% Brij-35,  
575 400mM 40mM EDTA pH 7.5), 8 nM ADP Alexa Fluor 594 Tracer and 93.7 µg/mL ADP2  
576 Antibody IRDye QC-1, covered and incubated at 20°C for 1 hr before reading the  
577 fluorescence. The fluorescence intensity was measured using a SpectraMax M5 plate  
578 reader at excitation 590 nm and emission 620 nm. All data was normalized against the  
579 appropriate measurements obtained for 100 µM ATP and 100 µM ADP with no kinase.  
580 The percent ATP turnover was interpolated using a standard curve (0.1-100 µM ADP).  
581 Interpolated values were then used to calculate the specific activity of the enzyme.

582

### 583 *Biolayer interferometry*

584 All Biolayer interferometry experiments were performed using the Octet K2  
585 instrument (Fortebio Inc.). For all experiments His-tagged nanobody (500 nM) was  
586 immobilized on an Anti-Penta-His biosensor for 600s, and the sensor was dipped into  
587 varying concentrations of the protein complex being measured. A dose response was  
588 carried out for p110γ, p110γ-p84, and p110γ-p101 (50 nM – 1.9 nM), with association  
589 occurring for 600s, followed by a 1200s dissociation in Octet Buffer (20 mM tris pH 8.5,  
590 100 mM NaCl, 50 mM ammonium sulfate, 0.1% bovine serum albumin, and 0.02%  
591 Tween 20). Experiments comparing class IA PI3K versus class IB PI3K used 50 nM of  
592 each class IA PI3K.

593           When comparing nanobody binding to phosphorylated and unphosphorylated  
594 p110 $\gamma$ , we used a final concentration of 25 nM for both phosphorylated and non-  
595 phosphorylated p110 $\gamma$  with association occurring for 600s, followed by a 600s  
596 dissociation. The  $K_D$  (dissociation constant) for the different p110 $\gamma$  complexes was  
597 calculated from the binding curves based on their global fit to a 1:1 binding model using  
598 ForteBio data analysis 12.0 (ForteBio Inc.).

599

#### 600 *Supported lipid bilayer TIRF microscopy experiments*

601           The membrane binding dynamics of Dy647-p84-p110 $\gamma$  were measured in the  
602 absence and presence of nanobody 7 (NB7) using TIRF microscopy. As previously  
603 described (Rathinaswamy et al., 2023), supported lipid bilayers were formed using 50  
604 nm extruded small unilamellar vesicles (SUVs) containing the following lipids: 1,2-  
605 dioleoyl-sn-glycero-3-phosphocholine (18:1 DOPC, Avanti # 850375C), 1,2-dioleoyl-sn-  
606 glycero-3-phospho-L-serine (18:1 DOPS, Avanti # 840035C), 1,2-dioleoyl-sn-glycero-3-  
607 phosphoethanolamine-N-[4-(p-maleimidomethyl)cyclohexane-carboxamide] (18:1 MCC-  
608 PE, Avanti # 780201C). Lipid compositions reported in figure legends represent the  
609 molar percentage of each lipid species.

610           To create SLBs, a total concentration of 0.25 mM lipids was solvated in 1x PBS  
611 [pH 7.4] and deposited on Piranha etched glass coverslips (25 x 75 mm) adhered to an  
612 IBIDI chamber. After a 30-minute incubation, membranes were washed with 4 mL of 1x  
613 PBS [pH 7.4] and then blocked for 10 minutes with 1 mg/mL beta casein (Thermo  
614 FisherSci, Cat# 37528) in 1x PBS [pH 7.4] (Corning, Cat# 46-013-CM). To conjugate H-  
615 Ras to maleimide lipids (MCC-PE), blocked membranes were incubated with 30  $\mu$ M H-  
616 Ras (GDP) in buffer containing 1x PBS [pH 7.4], 1 mM MgCl<sub>2</sub>, 50  $\mu$ M GDP, and 0.1 mM  
617 TCEP for 2 hours. The membrane conjugation reaction was terminated after 2 hours  
618 with 1x PBS [pH 7.4] containing 5 mM  $\beta$ -mercaptoethanol ( $\beta$ ME). Membranes were then  
619 washed and stored in 1x PBS [pH 7.4] until performing the TIRF-M membrane binding  
620 experiments. H-Ras was purified as previously described (Rathinaswamy et al., 2023).

621           To perform the TIRF-M membrane binding assays, 200 nM farnesyl- $G\beta\gamma$  was  
622 equilibrated into the supported membranes for 30 minutes. In parallel, nucleotide  
623 exchange of H-Ras (GDP) was performed by adding 50 nM guanine nucleotide

624 exchange factor (SosCat) in 1x PBS [pH 7.4], 1 mM MgCl<sub>2</sub>, 50 μM GDP. To measure  
625 membrane binding, Dy647-p84-p110γ was diluted into the following buffer: 20 mM  
626 HEPES [pH 7.0], 150 mM NaCl, 50 μM GTP, 1 mM ATP, 5 mM MgCl<sub>2</sub>, 0.5 mM EGTA,  
627 20 mM glucose, 200 μg/mL beta casein (ThermoScientific, Cat# 37528), 20 mM BME,  
628 320 μg/mL glucose oxidase (Serva, #22780.01 *Aspergillus niger*), 50 μg/mL catalase  
629 (Sigma, #C40-100MG Bovine Liver), and 2 mM Trolox. Trolox was prepared as  
630 previously described (Hansen et al., 2019). Perishable reagents (i.e., glucose oxidase,  
631 catalase, and Trolox) were added 10 minutes before image acquisition.

632 TIRF-M experiments were performed using an inverted Nikon Ti2 microscope  
633 with a 100x Nikon (1.49 NA) oil immersion objective. The x-axis and y-axis positions  
634 were controlled using a Nikon motorized stage. Dy647-p84-p110γ was excited with a  
635 637 nm diode laser (OBIS laser diode, Coherent Inc. Santa Clara, CA) controlled with  
636 an acousto-optic tunable filter (AOTF) and laser launch built by Vortran (Sacramento,  
637 CA). The power output measured through the objective for single particle imaging was  
638 1-3 mW. Excitation light passing through quad multi-pass dichroic filter cube (Semrock).  
639 Fluorescence emission passed through Nikon emission filter wheel containing the  
640 following 25 mm ET700/75M emission filters (Semrock) before being detected on iXion  
641 Life 897 EMCCD camera (Andor Technology Ltd., UK). All TIRF-M experiments were  
642 performed at room temperature (23°C). Microscope hardware was controlled using  
643 Nikon NIS elements. Data analysis was performed using ImageJ/Fiji and Prism  
644 graphing program.

645

#### 646 *Cryo-EM Sample Preparation and Data Collection*

647 3 μL of purified nanobody-bound p110γ at 0.45 mg/ml was adsorbed onto C-Flat  
648 2/2-T grids that were glow discharged for 25 s at 15 mA. Grids were then plunged into  
649 liquid ethane using a Vitrobot Mark IV (Thermo Fisher Scientific) with the following  
650 settings: -5 blot force, 1.5 s blot time, 100% humidity and 4 °C. Vitrified specimens were  
651 screened for ice and particle quality at the UBC High resolution macromolecular  
652 electron microscopy (HRMEM) facility using a 200-kV Glacios transmission electron  
653 microscope equipped with a Falcon 3EC direct electron detector (DED). Clipped grids  
654 were sent to the Pacific Northwest Cryo-EM Center (PNCC) where 7,322 movies were



655 collected using a Titan Krios equipped with a Gatan K3 DED and a BioQuantum K3  
656 energy filter with a slit width of 20 eV. The movies were collected at a physical pixel size  
657 of 0.830 Å/pix and a total dose of 50e<sup>-</sup>/Å<sup>2</sup> over 50 frames.

658

### 659 *Cryo-EM image analysis*

660 The data were processed using cryoSPARC v.3.3.2 (Punjani et al., 2017). The  
661 movies were pre-processed by patch motion correction using default settings except  
662 Fourier-cropping by a factor of 2, followed by patch CTF estimation using default  
663 settings. A 3D map of PI3K p110γ-p101 complex (EMD-23808) was used to create 2D  
664 projections for use as templates to auto-pick 1,463,553 particles. Particles were  
665 extracted with a box size of 380 pixels, Fourier cropped to a box size of 96 pixels and  
666 subjected to 2D classification. After discarding classes with obvious noise and no  
667 features, 795,162 particles were used for multiple rounds of *ab initio* reconstruction and  
668 heterogeneous refinement using 4 or 5 classes. 365,178 particles, which generated the  
669 two best 3D reconstruction, were used to carry out Per-particle local-motion correction  
670 with 760 pixels box size later downsized to 380 pixels followed by several rounds of *ab*  
671 *initio* reconstruction and heterogeneous refinement using 3 or 5 classes. 149,603 from  
672 best class were further refined by homogeneous refinement and a final Non-Uniform  
673 (NU)-refinement which generated a reconstruction with an overall resolution of 3.02 Å  
674 based on the Fourier shell correlation (FSC) 0.143 criterion.

675

### 676 *Building the structural model of p110γ-NB7*

677 The previous structural model of full length p110γ from the complex of p110γ-  
678 p101(PDB: 7MEZ) (Rathinaswamy et al., 2021a) was fit into the map using Chimera  
679 (Pettersen et al., 2004). A model of the nanobody was generated using Alphafold2  
680 using the Colabfold v1.5.2 server (Mirdita et al., 2022). The CDR loops were removed  
681 from this initial model, and the remaining nanobody was fit into the map using Chimera.  
682 The final structure was built by iterative rounds of automated model building in Phenix,  
683 manual model building in COOT (Emsley et al., 2010), and refinement in  
684 Phenix.real\_space\_refine using realspace, rigid body, and adp refinement with tight



685 secondary structure restraints (Afonine et al., 2012). This allowed for unambiguous  
686 building of the CDRs of the nanobody, and their interface with p110 $\gamma$ . The full refinement  
687 and validation statistics are shown in Supplemental table 1.

688

### 689 *Phosphorylation analysis*

690 For the dose–response phosphorylation of p110 $\gamma$ , p110/p84, and p110/p101,  
691 each protein or complex (750nM) was mixed with ATP (200  $\mu$ M), GFB (20mM Tris pH  
692 8.5, 100 mM NaCl, 50 mM Ammonium Sulfate and 0.5 mM TCEP), MgCl<sub>2</sub> (20mM) and  
693 various amounts of PKC $\beta$  (4  $\mu$ g, 800 ng, 160 ng, 32 ng, 6.4 ng, and 0 ng). Reactions  
694 were incubated for three hours on ice and quenched with 50  $\mu$ L of ice-cold acidic  
695 quench buffer (0.7 M guanidine-HCl, 1% formic acid). followed by immediate freezing  
696 using liquid nitrogen and storage at –80 °C.

697 For the experiment studying the effect of nanobody on phosphorylation, p110 $\gamma$  or  
698 p110/p101, (500nM) was mixed with ATP (1 mM), GFB (20mM Tris pH 8.5, 100 mM  
699 NaCl, 50 mM Ammonium Sulfate and 0.5 mM TCEP), MgCl<sub>2</sub>(20mM), with nanobody  
700 and PKC $\beta$  present at 1200 nM and 500nM, respectively. Reactions were incubated for  
701 one hour at room temperature and quenched with 54  $\mu$ L of ice-cold acidic quench buffer  
702 (0.7 M guanidine-HCl, 1% formic acid) followed by immediate freezing using liquid  
703 nitrogen and storage at –80 °C.

704 Phosphorylation of all proteins was confirmed using Mass spectrometry and  
705 PEAKS7 analysis. The LC-MS analysis of these samples was carried out using the  
706 same pipeline as used in the HDX-MS section. The phosphorylated and non-  
707 phosphorylated peptide ratios were determined by generating extracted ion  
708 chromatograms for each phosphorylated or non-phosphorylated peptide using their  
709 molecular formula and charge state in the Bruker Compass Data Analysis software. The  
710 area under each extracted curve was then extracted. The full MS quantification of each  
711 of the phosphorylated and non-phosphorylated peptide is provided in the source data.

712

### 713 *Hydrogen Deuterium eXchange Mass Spectrometry*

714 Exchange reactions to assess differences in p110 $\gamma$  upon phosphorylation were  
715 carried out at 20°C in 10  $\mu$ L volumes with final concentrations of 1.6  $\mu$ M for both apo

716 and phosphorylated p110 $\gamma$ . A total of two conditions were assessed: p110 $\gamma$  apo and  
717 PKC $\beta$  phosphorylated p110 $\gamma$ . The hydrogen-deuterium exchange reaction was initiated  
718 by the addition of 8  $\mu$ L D<sub>2</sub>O buffer (94.3% D<sub>2</sub>O, 100 mM NaCl, 20 mM HEPES pH 7.5)  
719 to the 2  $\mu$ L protein for a final D<sub>2</sub>O concentration of 75.4%. Exchange was carried out  
720 over five time points (3s on ice, and 3s, 30s, 300s and 3000s at 20°C) and the reaction  
721 was quenched with addition of 60  $\mu$ L of ice-cold acidic quench buffer (0.7 M guanidine-  
722 HCl, 1% formic acid). After quenching, samples were immediately frozen in liquid  
723 nitrogen and stored at -80°C. All reactions were carried out in triplicate.

724  
725 *Protein Digestion and MS/MS Data Collection:* Protein samples for both HDX-MS  
726 and phosphorylation analysis were analyzed using the same LC-MS setup. Samples  
727 were rapidly thawed and injected onto an integrated fluidics system containing a HDx-3  
728 PAL liquid handling robot and climate-controlled chromatography system (LEAP  
729 Technologies), a Dionex Ultimate 3000 UHPLC system, as well as an Impact HD QTOF  
730 Mass spectrometer (Bruker). The protein was run over two immobilized pepsin columns  
731 (Applied Biosystems; Poroszyme™ Immobilized Pepsin Cartridge, 2.1 mm x 30 mm;  
732 Thermo-Fisher 2□3131□00; at 10°C and 2°C respectively) at 200  $\mu$ L/min for 3 minutes.  
733 The resulting peptides were collected and desalted on a C18 trap column [Acquity  
734 UPLC BEH C18 1.7 mm column (2.1 x 5 mm); Waters 186003975]. The trap was  
735 subsequently eluted in line with an ACQUITY 1.7  $\mu$ m particle, 100 x 1 mm<sup>2</sup> C18 UPLC  
736 column (Waters 186002352), using a gradient of 3-35% B (buffer A, 0.1% formic acid;  
737 buffer B, 100% acetonitrile) over 11 min immediately followed by a gradient of 35-80% B  
738 over 5 minutes. MS experiments acquired over a mass range from 150 to 2200  
739 mass/charge ratio (m/z) using an electrospray ionization source operated at a  
740 temperature of 200°C and a spray voltage of 4.5 kV.

741  
742 *Peptide Identification:* Peptides were identified using data-dependent acquisition  
743 following tandem MS/MS experiments (0.5 s precursor scan from 150□2000 m/z; twelve  
744 0.25 s fragment scans from 150-2000 m/z). MS/MS datasets were analyzed using  
745 PEAKS7 (PEAKS), and a false discovery rate was set at 0.1% using a database of  
746 purified proteins and known contaminants. The same approach was used to identify

747 phosphorylated and non-phosphorylated peptides for our in-vitro phosphorylation  
748 experiments, with variable phosphorylation of STY residues was added to the search.  
749 The search parameters were set with a precursor tolerance of 20 parts per million,  
750 fragment mass error 0.02 Da, and charge states from 1 to 8, with a selection criterion of  
751 peptides that had a  $-10\log P$  score of  $>24.03$  for phosphorylated and  $>23.05$  for non-  
752 phosphorylated. The MS/MS spectra of the PKC $\beta$  phosphorylated peptides are included  
753 in Fig S4.

754  
755 *Mass Analysis of Peptide Centroids and Measurement of Deuterium*  
756 *Incorporation:* HD-Examiner Software (Sierra Analytics) was used to automatically  
757 calculate the level of deuterium incorporation into each peptide. All peptides were  
758 manually inspected for correct charge state, correct retention time, and appropriate  
759 selection of isotopic distribution. Deuteration levels were calculated using the centroid of  
760 the experimental isotope clusters. HDX-MS results are presented with no correction for  
761 back exchange shown in the Source data, with the only correction being applied  
762 correcting for the deuterium oxide percentage of the buffer used in the exchange  
763 (75.4%). Changes in any peptide at any time point greater than specified cut-offs (5%  
764 and 0.45 Da) and with an unpaired, two-tailed t-test value of  $p < 0.01$  was considered  
765 significant. A number of peptides in the helical domain showed isotope distributions  
766 consistent with EX1 H/D exchange. Attempts to define the relative percentages of each  
767 population using HDExaminer were extremely noisy, so representative EX1 profiles are  
768 shown in Fig. 4C. The raw peptide deuterium incorporation graphs for a selection of  
769 peptides with significant differences are shown in Fig. 4D, with the raw data for all  
770 analysed peptides in the source data. To allow for visualization of differences across all  
771 peptides, we utilized number of deuterium difference (#D) plots (Fig. 4B). These plots  
772 show the total difference in deuterium incorporation over the entire H/D exchange time  
773 course, with each point indicating a single peptide. The data analysis statistics for all  
774 HDX-MS experiments are in Supplemental Table 2 according to the guidelines of  
775 (Masson et al., 2019). The mass spectrometry proteomics data have been deposited to  
776 the ProteomeXchange Consortium via the PRIDE partner repository (Perez-Riverol et  
777 al., 2022) with the dataset identifier PXD040765.

778

## 779 **References**

- 780 Afonine PV, Grosse-Kunstleve RW, Echols N, Headd JJ, Moriarty NW, Mustyakimov M,  
781 Terwilliger TC, Urzhumtsev A, Zwart PH, Adams PD. 2012. Towards automated  
782 crystallographic structure refinement with phenix.refine. *Acta Crystallogr D Biol*  
783 *Crystallogr* **68**:352–367. doi:10.1107/S0907444912001308
- 784 Angulo I, Vadas O, Garçon F, Banham-Hall E, Plagnol V, Leahy TR, Baxendale H,  
785 Coulter T, Curtis J, Wu C, Blake-Palmer K, Perisic O, Smyth D, Maes M, Fiddler  
786 C, Juss J, Cilliers D, Markelj G, Chandra A, Farmer G, Kielkowska A, Clark J,  
787 Kracker S, Debré M, Picard C, Pellier I, Jabado N, Morris JA, Barcenas-Morales  
788 G, Fischer A, Stephens L, Hawkins P, Barrett JC, Abinun M, Clatworthy M,  
789 Durandy A, Doffinger R, Chilvers ER, Cant AJ, Kumararatne D, Okkenhaug K,  
790 Williams RL, Condliffe A, Nejentsev S. 2013. Phosphoinositide 3-kinase  $\delta$  gene  
791 mutation predisposes to respiratory infection and airway damage. *Science*  
792 **342**:866–871. doi:10.1126/science.1243292
- 793 Becattini B, Marone R, Zani F, Arsenijevic D, Seydoux J, Montani J, Dulloo A, Thorens  
794 B, Preitner F, Wymann M, Solinas G. 2011. PI3Kgamma within a  
795 nonhematopoietic cell type negatively regulates diet-induced thermogenesis and  
796 promotes obesity and insulin resistance. *Proc Natl Acad Sci USA* **108**:E854-63.  
797 doi:10.1073/pnas.1106698108/-/DCSupplemental
- 798 Bell K, Sunose M, Ellard K, Cansfield A, Taylor J, Miller W, Ramsden N, Bergamini G,  
799 Neubauer G. 2012. SAR studies around a series of triazolopyridines as potent  
800 and selective PI3K $\gamma$  inhibitors. *Bioorg Med Chem Lett* **22**:5257–5263.  
801 doi:10.1016/j.bmcl.2012.06.049
- 802 Bohnacker T, Marone R, Collmann E, Calvez R, Hirsch E, Wymann M. 2009.  
803 PI3Kgamma adaptor subunits define coupling to degranulation and cell motility  
804 by distinct PtdIns(3,4,5)P<sub>3</sub> pools in mast cells. *Sci Signal* **2**:ra27.  
805 doi:10.1126/scisignal.2000259
- 806 Bohnacker T, Prota AE, Beaufils F, Burke JE, Melone A, Inglis AJ, Rageot D, Sele AM,  
807 Cmiljanovic V, Cmiljanovic N, Bargsten K, Aher A, Akhmanova A, Díaz JF,  
808 Fabbro D, Zvelebil M, Williams RL, Steinmetz MO, Wymann MP. 2017.  
809 Deconvolution of Buparlisib's mechanism of action defines specific PI3K and  
810 tubulin inhibitors for therapeutic intervention. *Nat Commun* **8**:14683.  
811 doi:10.1038/ncomms14683
- 812 Breasson L, Becattini B, Sardi C, Molinaro A, Zani F, Marone R, Botindari F,  
813 Bousquenaud M, Ruegg C, Wymann MP, Solinas G. 2017. PI3K $\gamma$  activity in  
814 leukocytes promotes adipose tissue inflammation and early-onset insulin  
815 resistance during obesity. *Sci Signal* **10**:eaaf2969. doi:10.1126/scisignal.aaf2969
- 816 Burke JE. 2018. Structural Basis for Regulation of Phosphoinositide Kinases and Their  
817 Involvement in Human Disease. *Mol Cell* **71**:653–673.  
818 doi:10.1016/j.molcel.2018.08.005
- 819 Burke JE, Perisic O, Masson GR, Vadas O, Williams RL. 2012. Oncogenic mutations  
820 mimic and enhance dynamic events in the natural activation of phosphoinositide  
821 3-kinase p110 $\alpha$  (PIK3CA). *Proc Natl Acad Sci USA* **109**:15259–15264.  
822 doi:10.1073/pnas.1205508109

- 823 Burke JE, Vadas O, Berndt A, Finegan T, Perisic O, Williams RL. 2011. Dynamics of the  
824 phosphoinositide 3-kinase p110 $\delta$  interaction with p85 $\alpha$  and membranes reveals  
825 aspects of regulation distinct from p110 $\alpha$ . *Structure* **19**:1127–1137.  
826 doi:10.1016/j.str.2011.06.003
- 827 Burke JE, Williams RL. 2015. Synergy in activating class I PI3Ks. *Trends in Biochemical*  
828 *Sciences* **40**:88–100. doi:10.1016/j.tibs.2014.12.003
- 829 Burke JE, Williams RL. 2013. Dynamic steps in receptor tyrosine kinase mediated  
830 activation of class IA phosphoinositide 3-kinases (PI3K) captured by H/D  
831 exchange (HDX-MS). *Adv Biol Regul* **53**:97–110. doi:10.1016/j.jbior.2012.09.005
- 832 Campa CC, Silva RL, Margaria JP, Pirali T, Mattos MS, Kraemer LR, Reis DC, Grosa  
833 G, Copperi F, Dalmarco EM, Lima-Júnior RCP, Aprile S, Sala V, Dal Bello F,  
834 Prado DS, Alves-Filho JC, Medana C, Cassali GD, Tron GC, Teixeira MM,  
835 Ciraolo E, Russo RC, Hirsch E. 2018. Inhalation of the prodrug PI3K inhibitor  
836 CL27c improves lung function in asthma and fibrosis. *Nat Commun* **9**:5232–16.  
837 doi:10.1038/s41467-018-07698-6
- 838 Camps M, Rückle T, Ji H, Ardisson V, Rintelen F, Shaw J, Ferrandi C, Chabert C,  
839 Gillieron C, Françon B, Martin T, Gretener D, Perrin D, Leroy D, Vitte P-A, Hirsch  
840 E, Wymann MP, Cirillo R, Schwarz MK, Rommel C. 2005. Blockade of  
841 PI3K $\gamma$  suppresses joint inflammation and damage in mouse models of  
842 rheumatoid arthritis. *Nat Med* **11**:936–943. doi:10.1038/nm1284
- 843 De Henau O, Rausch M, Winkler D, Campesato LF, Liu C, Cymerman DH, Budhu S,  
844 Ghosh A, Pink M, Tchaicha J, Douglas M, Tibbitts T, Sharma S, Proctor J,  
845 Kosmider N, White K, Stern H, Soglia J, Adams J, Palombella VJ, McGovern K,  
846 Kutok JL, Wolchok JD, Merghoub T. 2016. Overcoming resistance to checkpoint  
847 blockade therapy by targeting PI3K $\gamma$  in myeloid cells. *Nature* **539**:443–447.  
848 doi:10.1038/nature20554
- 849 Deladeriere A, Gambardella L, Pan D, Anderson KE, Hawkins PT, Stephens LR. 2015.  
850 The regulatory subunits of PI3K $\gamma$  control distinct neutrophil responses. *Sci Signal*  
851 **8**:ra8. doi:10.1126/scisignal.2005564
- 852 Dornan GL, Siempelkamp BD, Jenkins ML, Vadas O, Lucas CL, Burke JE. 2017.  
853 Conformational disruption of PI3K $\delta$  regulation by immunodeficiency mutations in  
854 PIK3CD and PIK3R1. *Proc Natl Acad Sci USA* **114**:1982–1987.  
855 doi:10.1073/pnas.1617244114
- 856 Emsley P, Lohkamp B, Scott WG, Cowtan K. 2010. Features and development of Coot.  
857 *Acta Crystallogr D Biol Crystallogr* **66**:486–501.  
858 doi:10.1107/S0907444910007493
- 859 Evans CA, Liu T, Lescarbeau A, Nair SJ, Grenier L, Pradeilles JA, Glenadel Q, Tibbitts  
860 T, Rowley AM, DiNitto JP, Brophy EE, O'Hearn EL, Ali JA, Winkler DG, Goldstein  
861 SI, O'Hearn P, Martin CM, Hoyt JG, Soglia JR, Cheung C, Pink MM, Proctor JL,  
862 Palombella VJ, Tremblay MR, Castro AC. 2016. Discovery of a Selective  
863 Phosphoinositide-3-Kinase (PI3K)- $\gamma$  Inhibitor (IPI-549) as an Immuno-Oncology  
864 Clinical Candidate. *ACS Med Chem Lett* **7**:862–867.  
865 doi:10.1021/acsmchemlett.6b00238
- 866 Gangadhara G, Dahl G, Bohnacker T, Rae R, Gunnarsson J, Blaho S, Öster L,  
867 Lindmark H, Karabelas K, Pemberton N, Tyrchan C, Mogemark M, Wymann MP,  
868 Williams RL, Perry MWD, Papavoine T, Petersen J. 2019. A class of highly



- 869 selective inhibitors bind to an active state of PI3K $\gamma$ . *Nature Chemical Biology*  
870 **15**:348–357. doi:10.1038/s41589-018-0215-0
- 871 Hansen SD, Huang WYC, Lee YK, Bieling P, Christensen SM, Groves JT. 2019.  
872 Stochastic geometry sensing and polarization in a lipid kinase-phosphatase  
873 competitive reaction. *Proc Natl Acad Sci U S A* **116**:15013–15022.  
874 doi:10.1073/pnas.1901744116
- 875 Hawkins PT, Stephens LR. 2015. PI3K signalling in inflammation. *Biochim Biophys Acta*  
876 **1851**:882–897. doi:10.1016/j.bbali.2014.12.006
- 877 Jenkins ML, Ranga-Prasad H, Parson MAH, Harris NJ, Rathinaswamy MK, Burke JE.  
878 2023. Oncogenic mutations of PIK3CA lead to increased membrane recruitment  
879 driven by reorientation of the ABD, p85 and C-terminus. *Nat Commun* **14**:181.  
880 doi:10.1038/s41467-023-35789-6
- 881 Jin JR, Gogvadze E, Xavier AR, Bohnacker T, Voelzmann J, Wymann MP. 2020. PI3K $\gamma$   
882 Regulatory Protein p84 Determines Mast Cell Sensitivity to Ras Inhibition-Moving  
883 Towards Cell Specific PI3K Targeting? *Front Immunol* **11**:585070.  
884 doi:10.3389/fimmu.2020.585070
- 885 Johannessen CM, Boehm JS, Kim SY, Thomas SR, Wardwell L, Johnson LA, Emery  
886 CM, Stransky N, Cogdill AP, Barretina J, Caponigro G, Hieronymus H, Murray  
887 RR, Salehi-Ashtiani K, Hill DE, Vidal M, Zhao JJ, Yang X, Alkan O, Kim S, Harris  
888 JL, Wilson CJ, Myer VE, Finan PM, Root DE, Roberts TM, Golub T, Flaherty KT,  
889 Dummer R, Weber BL, Sellers WR, Schlegel R, Wargo JA, Hahn WC, Garraway  
890 LA. 2010. COT drives resistance to RAF inhibition through MAP kinase pathway  
891 reactivation. *Nature* **468**:968–972. doi:10.1038/nature09627
- 892 Kaneda MM, Cappello P, Nguyen AV, Ralainirina N, Hardamon CR, Foubert P, Schmid  
893 MC, Sun P, Mose E, Bouvet M, Lowy AM, Valasek MA, Sasik R, Novelli F, Hirsch  
894 E, Varner JA. 2016a. Macrophage PI3K $\gamma$  Drives Pancreatic Ductal  
895 Adenocarcinoma Progression. *Cancer Discov* **6**:870–885. doi:10.1158/2159-  
896 8290.CD-15-1346
- 897 Kaneda MM, Messer KS, Ralainirina N, Li H, Leem CJ, Gorjestani S, Woo G, Nguyen  
898 AV, Figueiredo CC, Foubert P, Schmid MC, Pink M, Winkler DG, Rausch M,  
899 Palombella VJ, Kutok J, McGovern K, Frazer KA, Wu X, Karin M, Sasik R, Cohen  
900 EEW, Varner JA. 2016b. PI3K $\gamma$  is a molecular switch that controls immune  
901 suppression. *Nature* **539**:437–442. doi:10.1038/nature19834
- 902 Kurig B, Shymanets A, Bohnacker T, Prajwal, Brock C, Ahmadian MR, Schaefer M,  
903 Gohla A, Harteneck C, Wymann MP, Jeanclos E, Nürnberg B. 2009. Ras is an  
904 indispensable coregulator of the class IB phosphoinositide 3-kinase  
905 p87/p110 $\gamma$ . *Proc Natl Acad Sci USA* **106**:20312–20317.  
906 doi:10.1073/pnas.0905506106
- 907 Laffargue M, Calvez R, Finan P, Trifilieff A, Barbier M, Altruda F, Hirsch E, Wymann  
908 MP. 2002. Phosphoinositide 3-kinase  $\gamma$  is an essential amplifier of mast  
909 cell function. *Immunity* **16**:441–451.
- 910 Lanahan SM, Wymann MP, Lucas CL. 2022. The role of PI3K $\gamma$  in the immune system:  
911 new insights and translational implications. *Nat Rev Immunol*.  
912 doi:10.1038/s41577-022-00701-8
- 913 Lawrence MS, Stojanov P, Mermel CH, Robinson JT, Garraway LA, Golub TR,  
914 Meyerson M, Gabriel SB, Lander ES, Getz G. 2014. Discovery and saturation

- 915 analysis of cancer genes across 21 tumour types. *Nature* **505**:495–501.  
916 doi:10.1038/nature12912
- 917 Li H, Prever L, Hirsch E, Gulluni F. 2021. Targeting PI3K/AKT/mTOR Signaling Pathway  
918 in Breast Cancer. *Cancers (Basel)* **13**:3517. doi:10.3390/cancers13143517
- 919 Li Z, Jiang H, Xie W, Zhang Z, Smrcka AV, Wu D. 2000. Roles of PLC-beta2 and -beta3  
920 and PI3Kgamma in chemoattractant-mediated signal transduction. *Science*  
921 **287**:1046–1049. doi:10.1126/science.287.5455.1046
- 922 Liu X, Zhou Q, Hart JR, Xu Y, Yang S, Yang D, Vogt PK, Wang M-W. 2022. Cryo-EM  
923 structures of cancer-specific helical and kinase domain mutations of PI3K $\alpha$ . *Proc*  
924 *Natl Acad Sci U S A* **119**:e2215621119. doi:10.1073/pnas.2215621119
- 925 Lucas CL, Kuehn HS, Zhao F, Niemela JE, Deenick EK, Palendira U, Avery DT, Moens  
926 L, Cannons JL, Biancalana M, Stoddard J, Ouyang W, Frucht DM, Rao VK,  
927 Atkinson TP, Agharahimi A, Hussey AA, Folio LR, Olivier KN, Fleisher TA,  
928 Pittaluga S, Holland SM, Cohen JI, Oliveira JB, Tangye SG, Schwartzberg PL,  
929 Lenardo MJ, Uzel G. 2014. Dominant-activating germline mutations in the gene  
930 encoding the PI(3)K catalytic subunit p110 $\delta$  result in T cell senescence and  
931 human immunodeficiency. *Nat Immunol* **15**:88–97. doi:10.1038/ni.2771
- 932 Luo L, Wall AA, Tong SJ, Hung Y, Xiao Z, Tarique AA, Sly PD, Fantino E, Marzolo M-P,  
933 Stow JL. 2018. TLR Crosstalk Activates LRP1 to Recruit Rab8a and PI3K $\gamma$  for  
934 Suppression of Inflammatory Responses. *Cell Rep* **24**:3033–3044.  
935 doi:10.1016/j.celrep.2018.08.028
- 936 Mandelker D, Gabelli SB, Schmidt-Kittler O, Zhu J, Cheong I, Huang C-H, Kinzler KW,  
937 Vogelstein B, Amzel LM. 2009. A frequent kinase domain mutation that changes  
938 the interaction between PI3K $\alpha$  and the membrane. *Proc Natl Acad Sci USA*  
939 **106**:16996–17001. doi:10.1073/pnas.0908444106
- 940 Masson GR, Burke JE, Ahn NG, Anand GS, Borchers C, Brier S, Bou-Assaf GM, Engen  
941 JR, Englander SW, Faber J, Garlish R, Griffin PR, Gross ML, Guttman M,  
942 Hamuro Y, Heck AJR, Houde D, Iacob RE, Jørgensen TJD, Kaltashov IA,  
943 Klinman JP, Konermann L, Man P, Mayne L, Pascal BD, Reichmann D, Skehel  
944 M, Snijder J, Strutzenberg TS, Underbakke ES, Wagner C, Wales TE, Walters  
945 BT, Weis DD, Wilson DJ, Wintrode PL, Zhang Z, Zheng J, Schriemer DC, Rand  
946 KD. 2019. Recommendations for performing, interpreting and reporting hydrogen  
947 deuterium exchange mass spectrometry (HDX-MS) experiments. *Nat Methods*  
948 **16**:595–602. doi:10.1038/s41592-019-0459-y
- 949 Miled N, Yan Y, Hon W-C, Perisic O, Zvelebil M, Inbar Y, Schneidman-Duhovny D,  
950 Wolfson HJ, Backer JM, Williams RL. 2007. Mechanism of two classes of cancer  
951 mutations in the phosphoinositide 3-kinase catalytic subunit. *Science* **317**:239–  
952 242. doi:10.1126/science.1135394
- 953 Mirdita M, Schütze K, Moriwaki Y, Heo L, Ovchinnikov S, Steinegger M. 2022.  
954 ColabFold: making protein folding accessible to all. *Nat Methods* **19**:679–682.  
955 doi:10.1038/s41592-022-01488-1
- 956 Okkenhaug K. 2013. Signaling by the phosphoinositide 3-kinase family in immune cells.  
957 *Annu Rev Immunol* **31**:675–704. doi:10.1146/annurev-immunol-032712-095946
- 958 Pacold ME, Suire S, Perisic O, Lara-Gonzalez S, Davis CT, Walker EH, Hawkins PT,  
959 Stephens L, Eccleston JF, Williams RL. 2000. Crystal structure and functional



- 960 analysis of Ras binding to its effector phosphoinositide 3-kinase gamma. *Cell*  
961 **103**:931–943.
- 962 Perez-Riverol Y, Bai J, Bandla C, García-Seisdedos D, Hewapathirana S,  
963 Kamatchinathan S, Kundu DJ, Prakash A, Frericks-Zipper A, Eisenacher M,  
964 Walzer M, Wang S, Brazma A, Vizcaíno JA. 2022. The PRIDE database  
965 resources in 2022: a hub for mass spectrometry-based proteomics evidences.  
966 *Nucleic Acids Res* **50**:D543–D552. doi:10.1093/nar/gkab1038
- 967 Perino A, Ghigo A, Ferrero E, Morello F, Santulli G, Baillie GS, Damilano F, Dunlop AJ,  
968 Pawson C, Walser R, Levi R, Altruda F, Silengo L, Langeberg LK, Neubauer G,  
969 Heymans S, Lembo G, Wymann MP, Wetzker R, Houslay MD, Iaccarino G, Scott  
970 JD, Hirsch E. 2011. Integrating Cardiac PIP(3) and cAMP Signaling through a  
971 PKA Anchoring Function of p110gamma. *Mol Cell* **42**:84–95.  
972 doi:10.1016/j.molcel.2011.01.030
- 973 Pettersen EF, Goddard TD, Huang CC, Couch GS, Greenblatt DM, Meng EC, Ferrin  
974 TE. 2004. UCSF Chimera--a visualization system for exploratory research and  
975 analysis. *J Comput Chem* **25**:1605–1612. doi:10.1002/jcc.20084
- 976 Punjani A, Rubinstein JL, Fleet DJ, Brubaker MA. 2017. cryoSPARC: algorithms for  
977 rapid unsupervised cryo-EM structure determination. *Nat Methods* **14**:290–296.  
978 doi:10.1038/nmeth.4169
- 979 Rathinaswamy MK, Burke JE. 2019. Class I phosphoinositide 3-kinase (PI3K)  
980 regulatory subunits and their roles in signaling and disease. *Adv Biol Regul*  
981 **100**:657. doi:10.1016/j.jbior.2019.100657
- 982 Rathinaswamy MK, Dalwadi U, Fleming KD, Adams C, Stariha JTB, Pardon E, Baek M,  
983 Vadas O, DiMaio F, Steyaert J, Hansen SD, Yip CK, Burke JE. 2021a. Structure  
984 of the phosphoinositide 3-kinase (PI3K) p110γ-p101 complex reveals molecular  
985 mechanism of GPCR activation. *Sci Adv* **7**:eabj4282. doi:10.1126/sciadv.abj4282
- 986 Rathinaswamy MK, Fleming KD, Dalwadi U, Pardon E, Harris NJ, Yip CK, Steyaert J,  
987 Burke JE. 2021b. HDX-MS-optimized approach to characterize nanobodies as  
988 tools for biochemical and structural studies of class IB phosphoinositide 3-  
989 kinases. *Structure* **29**:1371-1381.e6. doi:10.1016/j.str.2021.07.002
- 990 Rathinaswamy MK, Gaieb Z, Fleming KD, Borsari C, Harris NJ, Moeller BE, Wymann  
991 MP, Amaro RE, Burke JE. 2021c. Disease-related mutations in PI3Kγ disrupt  
992 regulatory C-terminal dynamics and reveal a path to selective inhibitors. *Elife*  
993 **10**:e64691. doi:10.7554/eLife.64691
- 994 Rathinaswamy MK, Jenkins ML, Duewell BR, Zhang X, Harris NJ, Evans JT, Stariha  
995 JTB, Dalwadi U, Fleming KD, Ranga-Prasad H, Yip CK, Williams RL, Hansen  
996 SD, Burke JE. 2023. Molecular basis for differential activation of p101 and p84  
997 complexes of PI3Kγ by Ras and GPCRs. *Cell Rep* **42**:112172.  
998 doi:10.1016/j.celrep.2023.112172
- 999 Rynkiewicz NK, Anderson KE, Suire S, Collins DM, Karanasios E, Vadas O, Williams R,  
1000 Oxley D, Clark J, Stephens LR, Hawkins PT. 2020. Gβγ is a direct regulator of  
1001 endogenous p101/p110γ and p84/p110γ PI3Kγ complexes in mouse neutrophils.  
1002 *Sci Signal* **13**:eaaz4003. doi:10.1126/scisignal.aaz4003
- 1003 Samuels Y, Wang Z, Bardelli A, Silliman N, Ptak J, Szabo S, Yan H, Gazdar A, Powell  
1004 S, Riggins G, Willson J, Markowitz S, Kinzler K, Vogelstein B, Velculescu V.

- 1005 2004. High frequency of mutations of the PIK3CA gene in human cancers.  
1006 *Science* **304**:554. doi:10.1126/science.1096502
- 1007 Shymanets A, Prajwal P, Bucher K, Beer-Hammer S, Harteneck C, Nürnberg B. 2013.  
1008 p87 and p101 subunits are distinct regulators determining class IB PI3K  
1009 specificity. *J Biol Chem* **288(43)**:31059–68. doi:10.1074/jbc.M113.508234
- 1010 Siempelkamp BD, Rathinaswamy MK, Jenkins ML, Burke JE. 2017. Molecular  
1011 mechanism of activation of class IA phosphoinositide 3-kinases (PI3Ks) by  
1012 membrane-localized HRas. *J Biol Chem* **292**:12256–12266.  
1013 doi:10.1074/jbc.M117.789263
- 1014 Stephens LR, Eguinoa A, Erdjument-Bromage H, Lui M, Cooke F, Coadwell J, Smrcka  
1015 AS, Thelen M, Cadwallader K, Tempst P, Hawkins PT. 1997. The Gbg sensitivity  
1016 of a PI3K is dependent upon a tightly associated adaptor, p101. *Cell* **89**:105–114.
- 1017 Takeda AJ, Maher TJ, Zhang Y, Lanahan SM, Bucklin ML, Compton SR, Tyler PM,  
1018 Comrie WA, Matsuda M, Olivier KN, Pittaluga S, McElwee JJ, Long Priel DA,  
1019 Kuhns DB, Williams RL, Mustillo PJ, Wymann MP, Koneti Rao V, Lucas CL.  
1020 2019. Human PI3K $\gamma$  deficiency and its microbiota-dependent mouse model  
1021 reveal immunodeficiency and tissue immunopathology. *Nat Commun* **10**:4364–  
1022 12. doi:10.1038/s41467-019-12311-5
- 1023 Vadas O, Dbouk HA, Shymanets A, Perisic O, Burke JE, Abi Saab WF, Khalil BD,  
1024 Harteneck C, Bresnick AR, Nürnberg B, Backer JM, Williams RL. 2013.  
1025 Molecular determinants of PI3K $\gamma$ -mediated activation downstream of G-protein-  
1026 coupled receptors (GPCRs). *Proc Natl Acad Sci U S A* **110**:18862–18867.  
1027 doi:10.1073/pnas.1304801110
- 1028 Vanhaesebroeck B, Perry MWD, Brown JR, André F, Okkenhaug K. 2021. PI3K  
1029 inhibitors are finally coming of age. *Nat Rev Drug Discov* **20**:741–769.  
1030 doi:10.1038/s41573-021-00209-1
- 1031 Vasan N, Cantley LC. 2022. At a crossroads: how to translate the roles of PI3K in  
1032 oncogenic and metabolic signalling into improvements in cancer therapy. *Nat*  
1033 *Rev Clin Oncol*. doi:10.1038/s41571-022-00633-1
- 1034 Walker EH, Perisic O, Ried C, Stephens L, Williams RL. 1999. Structural insights into  
1035 phosphoinositide 3-kinase catalysis and signalling. *Nature* **402**:313–320.  
1036 doi:10.1038/46319
- 1037 Walser R, Burke JE, Gogvadze E, Bohnacker T, Zhang X, Hess D, Küenzi P, Leitges M,  
1038 Hirsch E, Williams RL, Laffargue M, Wymann MP. 2013. PKC $\beta$  phosphorylates  
1039 PI3K $\gamma$  to activate it and release it from GPCR control. *PLoS Biol* **11**:e1001587.  
1040 doi:10.1371/journal.pbio.1001587
- 1041 Zhang X, Vadas O, Perisic O, Anderson KE, Clark J, Hawkins PT, Stephens LR,  
1042 Williams RL. 2011. Structure of lipid kinase p110 $\beta$ /p85 $\beta$  elucidates an unusual  
1043 SH2-domain-mediated inhibitory mechanism. *Mol Cell* **41**:567–578.  
1044 doi:10.1016/j.molcel.2011.01.026

1045  
1046  
1047  
1048

## Figures and Figure Legends

1049 **Figure 1. The inhibitory nanobody NB7 binds tightly to all p110 $\gamma$  complexes and inhibits kinase**  
1050 **activity, but does not prevent membrane binding**

1051 **A.** Cartoon schematic depicting nanobody inhibition of activation by lipidated G $\beta\gamma$  (1.5  $\mu$ M final  
1052 concentration) on 5% PIP<sub>2</sub> membrane (5% phosphatidylinositol 4,5-bisphosphate (PIP<sub>2</sub>), 95%  
1053 phosphatidylserine (PS)) activation. Lipid kinase assays showed a potent inhibition of lipid kinase activity  
1054 with increasing concentrations of NB7 (3-3000 nM) for the different complexes. Experiments are carried  
1055 out in triplicate (n=3) with each replicate shown. The y-axis shows lipid kinase activity normalised for each  
1056 complex activated by G $\beta\gamma$  in the absence of nanobody. Concentrations of each protein were selected to  
1057 give a lipid kinase value in the detectable range of the ATPase transcriber assay. The protein  
1058 concentration of p110 $\gamma$  (300 nM), p110 $\gamma$ -p84 (330 nM) and p110 $\gamma$ -p101 (12 nM) was different due to  
1059 intrinsic differences of each complex to be activated by lipidated G $\beta\gamma$  and is likely mainly dependent for  
1060 the difference seen in NB7 response.

1061 **B.** Association and dissociation curves for the dose response of His-NB7 binding to p110 $\gamma$ , p110 $\gamma$ -p84  
1062 and p110 $\gamma$ -p101 (50 – 1.9 nM) is shown. A cartoon schematic of BLI analysis of the binding of  
1063 immobilized His-NB7 to p110 $\gamma$  is shown on the left. Dissociation constants (K<sub>D</sub>) were calculated based on  
1064 a global fit to a 1:1 model for the top three concentrations and averaged with error shown. Error was  
1065 calculated from the association and dissociation value (n=3) with standard deviation shown. Full details  
1066 are present in the source data.

1067 **C.** Association and dissociation curves for His-NB7 binding to p110 $\gamma$ , p110 $\alpha$ -p85 $\alpha$ , p110 $\beta$ -p85 $\beta$ , and  
1068 p110 $\delta$ -p85 $\beta$ . Experiments were performed in duplicate with a final concentration of 50 nM of each class I  
1069 PI3K complex.

1070 **D.** Effect of NB7 on PI3K recruitment to supported lipid bilayers containing H-Ras (GTP) and farnesyl-G $\beta\gamma$   
1071 as measured by Total Internal Reflection Fluorescence Microscopy (TIRF-M). DY647-p84/p110 $\gamma$  displays  
1072 rapid equilibration kinetics and is insensitive to the addition of 500 nM nanobody (black arrow, 250 sec)  
1073 on supported lipid bilayers containing H-Ras (GTP) and farnesyl-G $\beta\gamma$ .

1074 **E.** Kinetics of 50 nM DY647-p84/p110 $\gamma$  membrane recruitment appears indistinguishable in the absence  
1075 and presence of nanobody. Prior to sample injection, DY647-p84/p110 $\gamma$  was incubated for 10 minutes  
1076 with 500 nM nanobody.

1077 **F.** Representative TIRF-M images showing the localization of 50 nM DY647-p84/p110 $\gamma$  visualized in the  
1078 absence or presence of 500 nM nanobody (+NB7). Membrane composition for panels C-E: 93% DOPC,  
1079 5% DOPS, 2% MCC-PE, Ras (GTP) covalently attached to MCC-PE, and 200 nM farnesyl-G $\beta\gamma$ .

1080

1081 **Figure 2. Structure of p110 $\gamma$  bound to inhibitory nanobody NB7**

1082 **A.** Domain schematics of p110 $\gamma$  with helical domain (blue), activation loop (orange), and regulatory motif  
1083 (green) of p110 $\gamma$  annotated.

1084 **B.** Cryo EM density of the p110 $\gamma$ -NB7 complex colored according to the schematic in **A**.

1085 **C.** Cartoon model of the structure of p110 $\gamma$  bound to NB7 colored according to **A**.

1086 **D.** Schematic depicting the key features of p110 $\gamma$  and the nanobody binding site, colored according to  
1087 panel **A**.

1088 **E.** Domain schematic of NB7 CDR regions and their sequences.

1089 **F.** Zoom in on the binding interface of NB7, with the CDRs colored as in panel E, and the electron  
1090 density of the CDR regions contoured at  $3\sigma$  (blue mesh).

1091  
1092 **Figure 3. PKC $\beta$  leads to dual phosphorylation of internal sites in the helical domain, with**  
1093 **selectivity for apo p110 $\gamma$  and p110 $\gamma$ -p84 over p110 $\gamma$ -p101.**

1094 **A.** Putative phosphorylation sites mapped on the structure of p110 $\gamma$  (PDB: 7MEZ) and cartoon schematic.  
1095 The regions are colored based on domain schematics featured in Fig 2A.

1096 **B.** Raw MS spectra of the unphosphorylated and phosphorylated peptide for a region spanning 579-592  
1097 (RYESLKHPKAYPKL) and 593-607 (FSSVKWGQQEIVAKT). The putative phosphorylation sites in the  
1098 sequence are shown in red, with the m/z theoretical (m/z t) and m/z experimental (m/z t) shown below  
1099 each sequence.

1100 **C-E.** Extracted traces and ratios of the intensity of extracted ion traces of different phosphorylation site  
1101 peptides (Top to bottom: S594/S595 and S582) from **(C)** p110 $\gamma$ , **(D)** p110 $\gamma$ /p84 or **(E)** p110 $\gamma$ /p101  
1102 samples treated with increasing concentration of PKC $\beta$  according to the legend. The black traces in the  
1103 ratio graphs are the intensity of the non-phosphorylated peptide, and the red traces in the ratio graphs are  
1104 the intensity of the phosphorylated peptide.

1105  
1106 **Figure 4. Activating phosphorylation at the helical domain leads to opening of the regulatory motif**

1107 **A.** HDX-MS comparing apo and phosphorylated p110 $\gamma$ . Significant differences in deuterium exchange  
1108 are mapped on to the structure and cartoon of p110 $\gamma$  according to the legend (PDB: 7MEZ).

1109 **B.** The graph of the #D difference in deuterium incorporation for p110 $\gamma$ , with each point representing a  
1110 single peptide. Peptides colored in red are those that had a significant change in the mutants (greater  
1111 than 0.4 Da and 5% difference at any timepoint, with a two tailed t-test  $p < 0.01$ ). Error bars are S.D. (n=3).

1112 **C.** Representative bimodal distribution (EX1 kinetics) observed in the helical domain peptides of p110 $\gamma$ .

1113 **D.** Representative p110 $\gamma$  peptides displaying increases in exchange in the phosphorylated state are  
1114 shown. For all panels, error bars show SD (n=3)

1115 **E.** Measurement of ATP to ADP conversion of phosphorylated and non-phosphorylated p110 $\gamma$  (1000 nM  
1116 final concentration) ATPase activity in the absence (left) and presence of PIP<sub>2</sub> membranes (5%  
1117 phosphatidylinositol 4,5-bisphosphate (PIP<sub>2</sub>), 95% phosphatidylserine (PS)) activation (right). Significance  
1118 is indicated by \*\*(<0.001%), and \*\*\*(<0.0001%).

1119

1120 **Figure 5. Nanobody NB7 blocks PKC $\beta$  phosphorylation, and phosphorylation prevents nanobody**  
1121 **binding.**

1122 **A.** Extracted ion chromatograms for p110 $\gamma$ , p110 $\gamma$ -p101, and p110 $\gamma$  bound to NB7 are shown for the  
1123 S594 or S595 phosphorylation site in p110 $\gamma$ . A bar graph showing the intensities of phosphorylated and  
1124 non-phosphorylated p110 $\gamma$  peptide (593-607) for p110 $\gamma$  (black), p110 $\gamma$  with NB7 (red) and p110 $\gamma$ p101  
1125 (purple) are shown to the right of the extracted ion chromatograms (n=3, right). In all experiments in  
1126 panels **A+B**, PKC $\beta$  was present at 500 nM. Significance is indicated by \*\*\*(<0.0001%).

1127 **B.** Extracted ion chromatograms for p110 $\gamma$ , p110 $\gamma$ -p101, and p110 $\gamma$  bound to NB7 are shown for the  
1128 S582 phosphorylation site in p110 $\gamma$ . A bar graph showing the intensities of phosphorylated and non-  
1129 phosphorylated p110 $\gamma$  peptide (579-592) p110 $\gamma$  (black), p110 $\gamma$  with NB7 (red) and p110 $\gamma$ -p101 (purple)  
1130 are shown to the right of the extracted ion chromatograms (n=3, right). Significance is indicated by \*  
1131 (<0.01%), and \*\*\*(<0.0001%). The putative phosphorylation site is shown in red in the sequence above  
1132 the bar graphs for both panel **A+B**.

1133 **C.** Cartoon schematic of BLI analysis of the binding of immobilized His-NB7 to phosphorylated and non-  
1134 phosphorylated p110 $\gamma$ .

1135 **D.** Association curves for phosphorylated and non-phosphorylated p110 $\gamma$  (25nM) binding to His-NB7 are  
1136 shown (n=3).

1137 **E.** ATPase kinase activity assays comparing the activation/inhibition of phosphorylated and non-  
1138 phosphorylated p110 $\gamma$  (1000 nM) with or without nanobody (3000 nM final) in the absence of PIP<sub>2</sub>  
1139 membranes. Significance is indicated by \* (<0.05%), and NS (>0.05%).

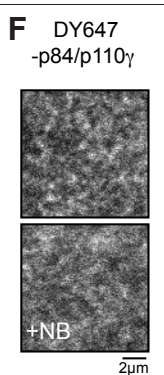
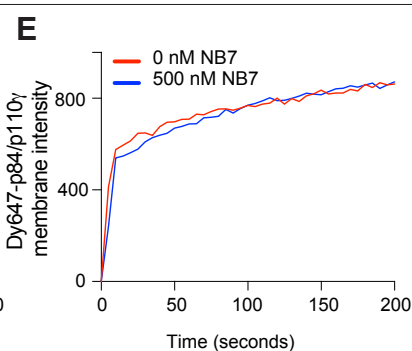
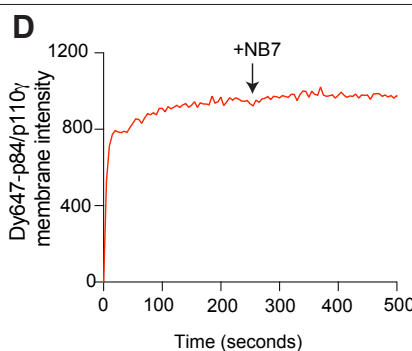
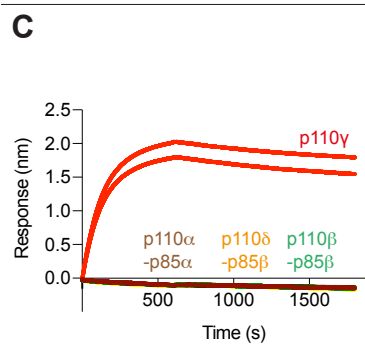
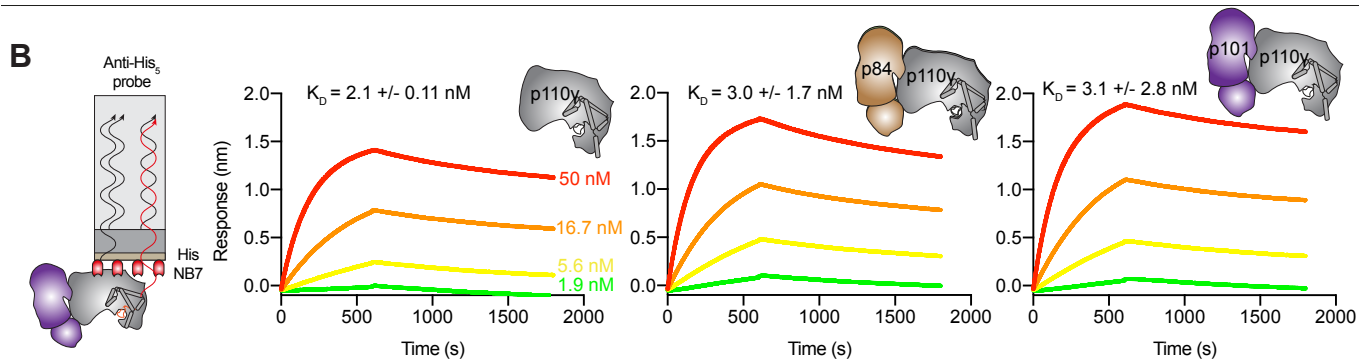
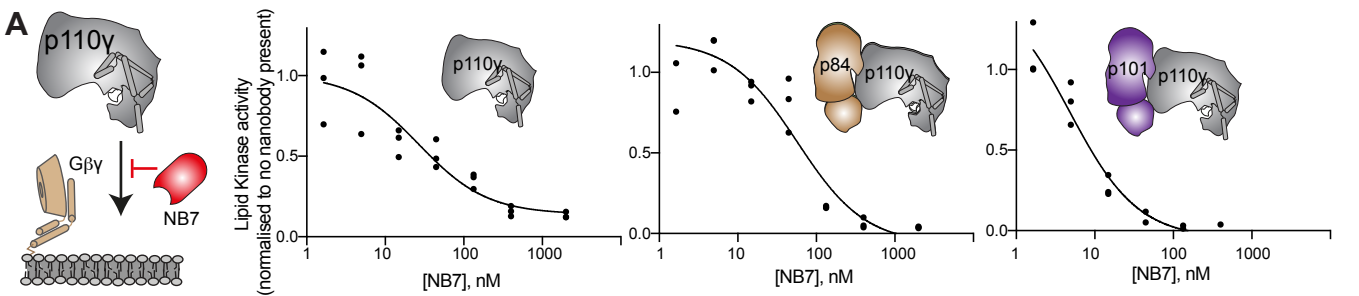
1140

1141 **Figure 6. Comparison of nanobody binding site compared to p85 inhibition of class IA PI3Ks and**  
1142 **class IB activation sites**

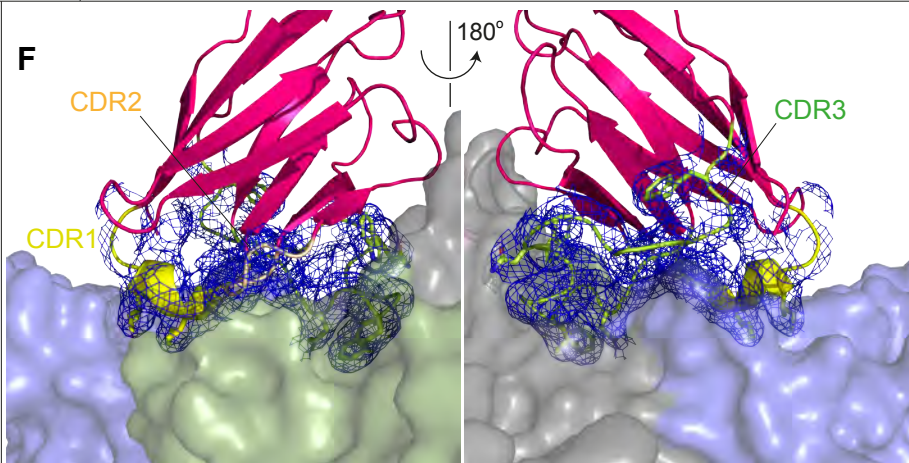
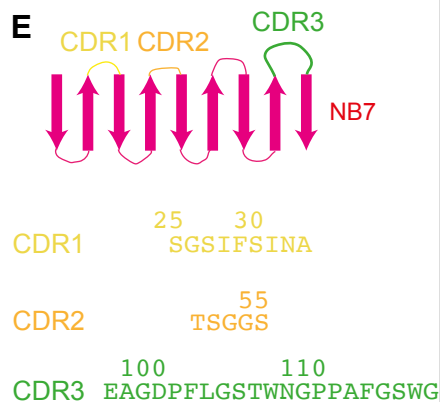
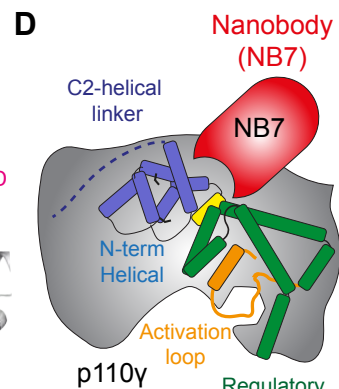
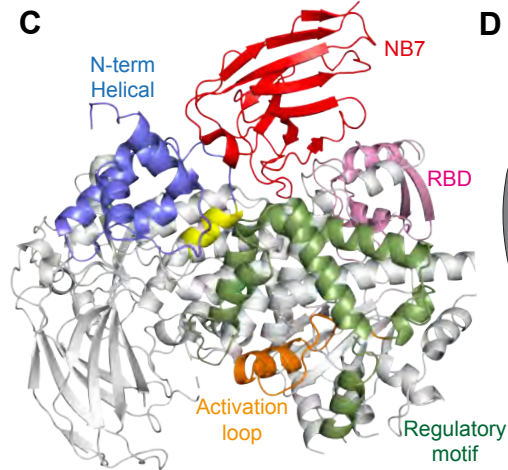
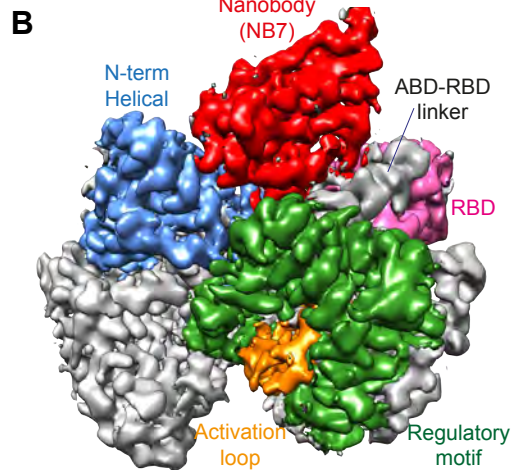
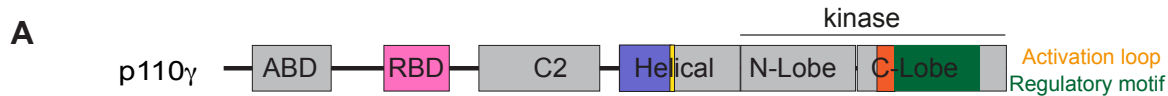
1143 **A.** Comparison of the nanobody NB7 binding site in p110 $\gamma$  compared to the nSH2 inhibitory site in p110 $\alpha$   
1144 (PDB: 3HHM) (Mandelker et al., 2009)

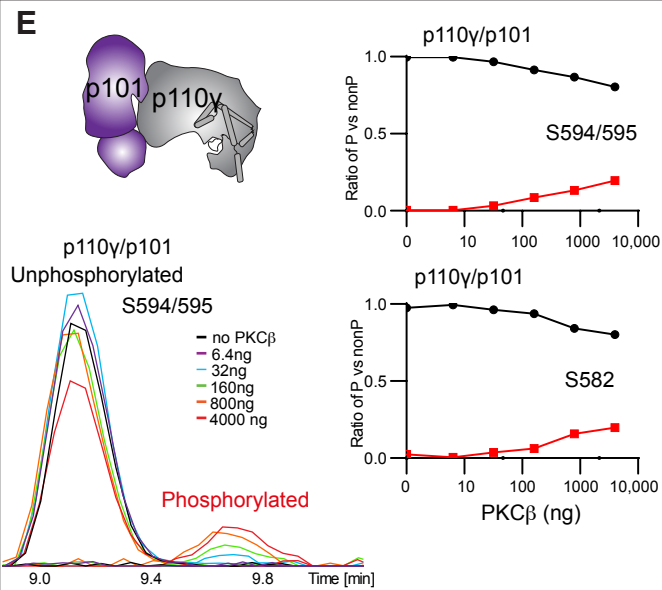
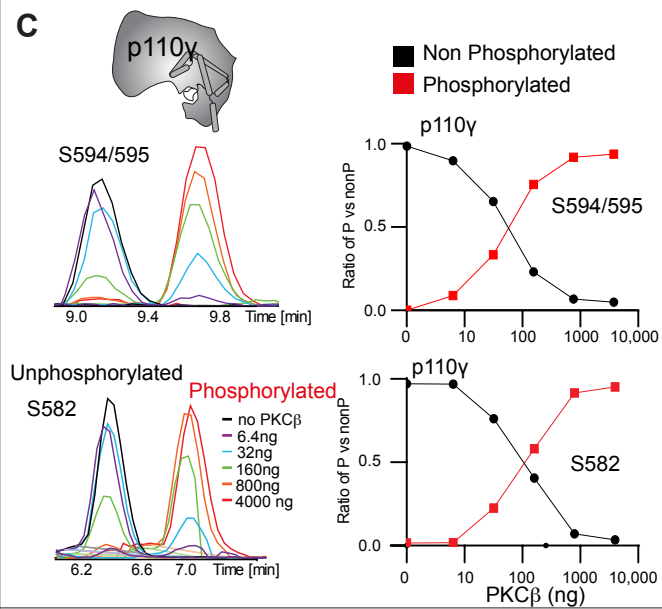
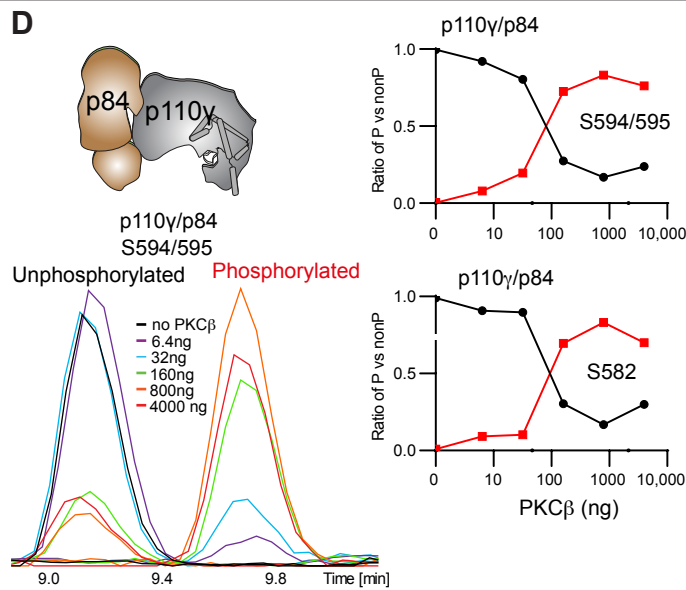
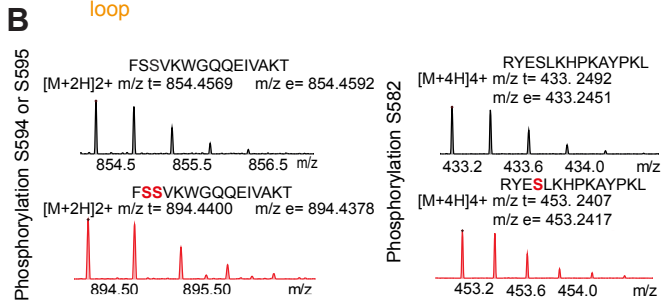
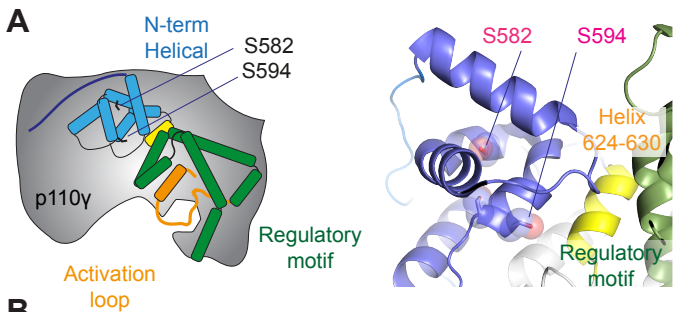
1145 **B.** Comparison of the nanobody NB7 binding site in p110 $\gamma$  compared to the X-ray structure of the Ras  
1146 binding site (PDB: 1HE8) (Pacold et al., 2000) and the AlphaFold model of G $\beta\gamma$  bound to p110 $\gamma$   
1147 (Rathinaswamy et al., 2023).

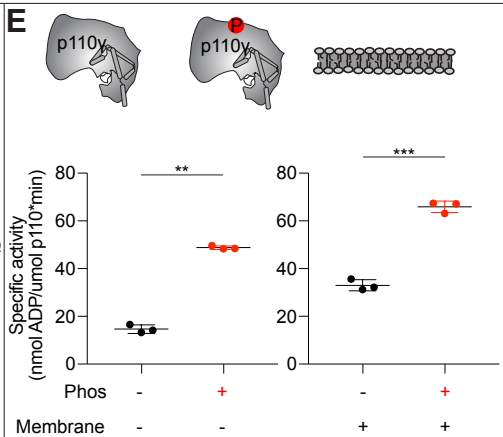
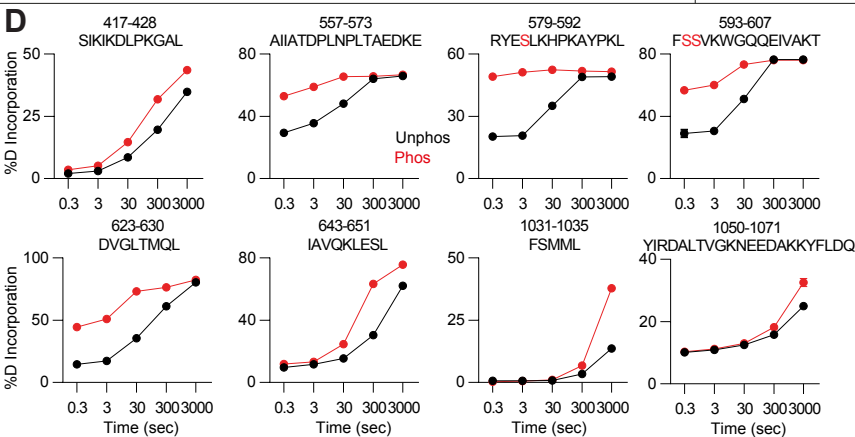
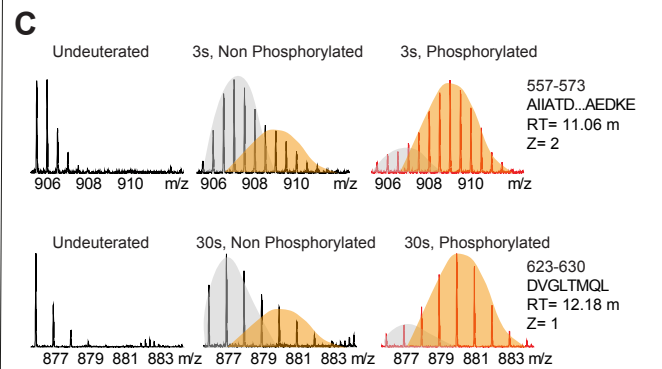
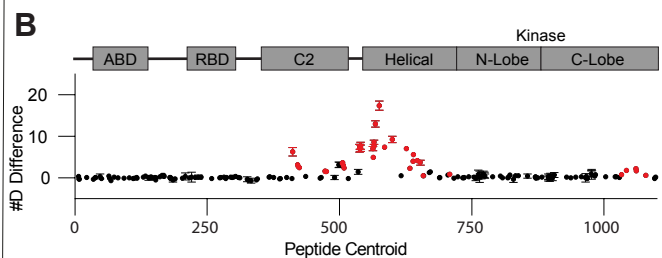
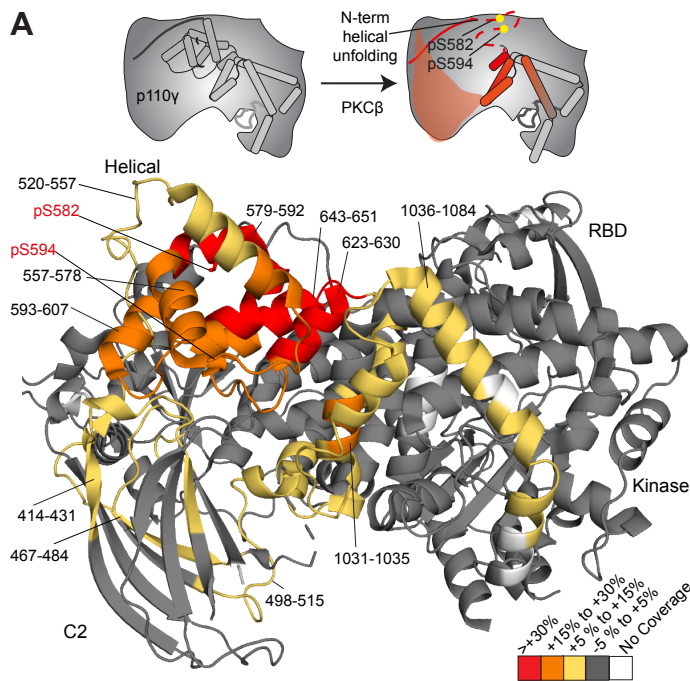
1148 **C.** Oncogenic mutations and post-translational modifications in spatial proximity to the nanobody binding  
1149 site.

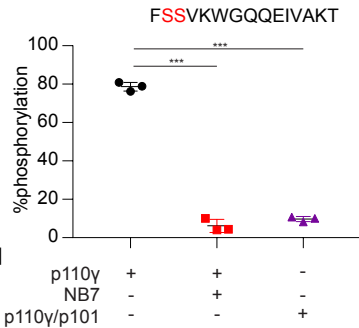
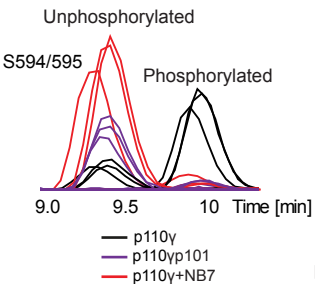
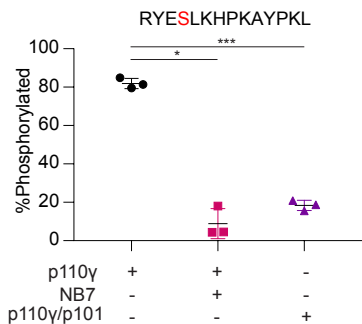
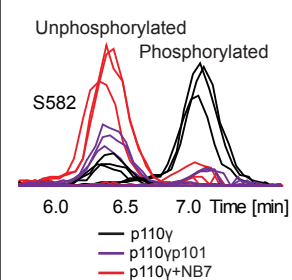
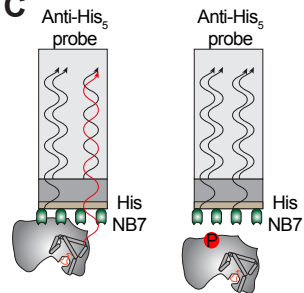
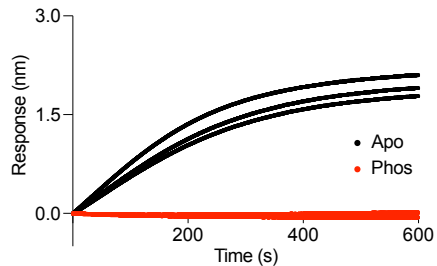










**A****B****C****D****E**